Error analysis for GNSS radio occultation data based on ensembles of profiles from end-to-end simulations

A. K. Steiner and G. Kirchengast

Wegener Center for Climate and Global Change (WegCenter) and Institute for Geophysics, Astrophysics, and Meteorology (IGAM), University of Graz, Graz, Austria

Received 19 July 2004; revised 25 April 2005; accepted 6 June 2005; published 13 August 2005.

[1] Radio occultation (RO) observations using the Global Navigation Satellite System (GNSS) globally provide high quality atmospheric data which can support the advancement of climate monitoring and modeling as well as the improvement of numerical weather prediction. In order to make optimal use of the data, e.g., via data assimilation systems, the characterization of measurement errors is of importance. Within this context we present results of an empirical error analysis based on quasi-realistically simulated GNSS RO data. The study is based on an end-to-end forward-inverse simulation involving (1) modeling of the neutral atmosphere and ionosphere, (2) simulation of RO observations, (3) forward modeling of excess phase observables including realistic observation system error modeling, and (4) retrieval of atmospheric parameters. Occultation observations were simulated for one day from which an ensemble of 300 occultation events was chosen, with 100 events in each of three latitude bands (low, middle, high). Phase path profiles were computed showing a realistic rms error of the ionosphere corrected phase paths of 2–3 mm at mesospheric and stratospheric heights at 10 Hz sampling rate. Atmospheric profiles were retrieved by applying a dry air retrieval in the stratosphere and an optimal estimation retrieval in the troposphere. The retrieved profiles were referenced to the "true" co-located ones of the analysis field of the European Centre for Medium-range Weather Forecasts (ECMWF). We empirically estimated bias profiles and covariance matrices (standard deviations and correlation functions) for the retrieval products such as bending angle, refractivity, pressure, geopotential height, temperature, and specific humidity. Results include the refractivity error showing a relative standard deviation of 0.1–0.75% and a relative bias of <0.1% at 5–40 km height. Temperature exhibits a standard deviation of 0.2–1 K at 3–31 km height and a bias of <0.1–0.5 K below 33 km and of <0.1 K below 20 km. Simple analytical error covariance formulations are presented for refractivity, as deduced from the empirically estimated covariance matrices. The reasonably realistic error estimates presented are a good basis for further retrieval algorithm improvements and for proper specification of observational errors in data assimilation systems.

Citation: Steiner, A. K., and G. Kirchengast (2005), Error analysis for GNSS radio occultation data based on ensembles of profiles from end-to-end simulations, *J. Geophys. Res.*, *110*, D15307, doi:10.1029/2004JD005251.

1. Introduction

[2] The GNSS RO technique is based on active limb sounding using a satellite-to-satellite radio link to probe the Earth's atmosphere. The GNSS-transmitted radio signals are influenced by the atmospheric and ionospheric refractivity field during their propagation to a receiver on a Low Earth Orbit (LEO) satellite. Observed excess phases (relative to propagation in vacuum) are the basis for high quality retrievals of atmospheric variables such as bending angle, refractivity, density, pressure, geopotential height, temperature, and water vapor as well as of ionospheric electron density.

0148-0227/05/2004JD005251$09.00

[3] Briefly, the processing proceeds along the following main steps. The time derivation of measured excess phase time series yields Doppler shift profiles. From the Doppler shift and from precise orbit information (satellite positions and velocities) bending angle profiles as function of impact parameter are derived. Ionospheric influences are removed by linear combination of the dual-frequency measurements either on phase path level or on bending angle level. A high altitude initialization of bending angle profiles is involved in order to prevent errors at mesospheric heights from degrading accuracy in the lower stratosphere. The retrieval of refractivity profiles from bending angles is based on the Abel inversion involving the assumption of local spherical symmetry about the profile location. Density, pressure, and temperature profiles can then be deduced from refractivity

employing the equation of state and the hydrostatic equation in a dry atmosphere (temperatures < 250 K). The retrieval of specific humidity and temperature profiles in the troposphere requires auxiliary background information. A detailed description of the data processing methodology is, e.g., provided by the review of *Kursinski et al.* [1997], complemented by the more technical description of *Hajj et al.* [2002].

[4] Originating from planetary radio science [e.g., *Fjeldbo and Eshleman*, 1965, 1969] the first practical application of the RO method to the terrestrial atmosphere was successfully demonstrated with the U.S. Global Positioning System Meteorology (GPS/MET) experiment [*Ware et al.*, 1996]. The strengths of the technique include all-weather capability, long-term stability, global coverage, and high accuracy and vertical resolution. Analysis and validation of GPS/MET data confirmed that the highest quality of the retrieved variables is achieved in the upper troposphere and lower stratosphere region with an (upper bound) accuracy in refractivity of <0.4%, in temperature of <1 K [*Kursinski et al.*, 1996, 1997; *Rocken et al.*, 1997; *Steiner et al.*, 1999], and in geopotential height of <20 m [*Leroy*, 1997]. The accuracy in specific humidity in the lower to middle troposphere is of the order 0.2–0.5 g/kg [*Kursinski and Hajj*, 2001].

[5] Ongoing GPS RO experiments are placed on board the German CHAMP satellite [*Reigber et al.*, 2002; *Wickert et al.*, 2001] and the Argentine SAC-C satellite [e.g., *Hajj et al.*, 2004]. The validation of CHAMP RO data with corresponding weather analyses profiles revealed an ensemble mean agreement of <0.4 K between 10–35 km height with a standard deviation of ~1 K at 10 km increasing to ~2 K at 30 km height [*Wickert et al.*, 2004]. The precision of RO data was investigated by *Hajj et al.* [2004], who performed an inter-comparison of nearby CHAMP and SAC-C temperature retrievals, which were found to be consistent to <0.1 K in the mean, and to 0.86 K in the standard deviation, between 5–15 km height.

[6] These results demonstrated the suitability of RO data for global climate monitoring and modeling and indicated their potential to make a vital contribution to the Global Climate Observing System [*GCOS*, 2003]. Such a contribution is studied by GNSS RO observing system simulation experiments (OSSE) [*Steiner et al.*, 2001; *Foelsche et al.*, 2003] and by climatological exploitation of RO data from GPS/MET [*Schroeder et al.*, 2003] and CHAMP [*Schmidt et al.*, 2004; *Foelsche et al.*, 2005]. It is planned to be fully realized by future RO constellation missions such as COSMIC [*Rocken et al.*, 2000; *Lee et al.*, 2001] and potentially ACE+ (Atmosphere and Climate Explorer) [*Hoeg and Kirchengast*, 2002; *Kirchengast and Hoeg*, 2004]. Regarding weather forecasting, *Kuo et al.* [2000] confirmed that the assimilation of RO data has the potential to significantly improve the accuracy of global and regional analysis and weather prediction, which is subject to investigation in assimilation studies [e.g., *Eyre*, 1994; *Zou et al.*, 2000; *Collard and Healy*, 2003; *Healy et al.*, 2005].

[7] One important issue in this respect is the knowledge on RO observation errors, which has also been addressed by *Kuo et al.* [2000] regarding the need for a better error characterization. *Syndergaard* [1999] investigated in a theoretical analysis the step-by-step covariance propagation from excess phase profiles via Doppler shift, bending angle, refractivity and pressure to temperature profiles. *Palmer et al.* [2000] presented an optimal estimation inverse method for the simultaneous retrieval of temperature, specific humidity and surface pressure from bending angle data with an error analysis emerging from the optimal estimation theory [*Rodgers*, 2000]. The practical application of this method to GPS/MET bending angles was carried out in a follow-on study by *Palmer and Barnett* [2001] including assumptions of simple background and measurement error covariances with correlations being neglected. A complete theoretical error analysis and characterization, based on optimal estimation methodology and accounting for error correlations, was performed by *Rieder and Kirchengast* [2001b]. Starting with excess phase error profiles, the properties of bending angle, refractivity, pressure, and dry temperature profiles were assessed and their covariance structure and correlation functions were analyzed.

[8] Within this context we present results of an ensemble-based empirical error analysis, which involves quasi-realistically simulated GNSS RO data and provides a complete error characterization for each retrieval product, including profiles of bending angle, refractivity, pressure, geopotential height, temperature, and specific humidity. The purpose of the work is to provide reasonably realistic error estimates of covariance matrices and, in addition to the above described previous studies, on bias profiles. Estimations of the latter are not possible with the optimal estimation approach [*Rodgers*, 2000], which could only linearly propagate pre-specified biases such as it propagates statistical errors [e.g., *Rieder and Kirchengast*, 2001b]. The present empirical approach, estimating the error statistics from Monte Carlo-type "retrieved-minus-true" profile ensembles, allows for both non-linearities and the natural emergence of biases throughout the end-to-end simulation chain, without the need for error pre-specifications.

[9] The study is based on an end-to-end forward-inverse simulation involving modeling of the neutral atmosphere and ionosphere and simulation of radio occultation events (section 2), forward modeling of excess phase observables including realistic observation system error modeling (section 3), and retrieval of atmospheric parameters (section 4). In section 5 a brief description of the error analysis scheme is given and the results of the empirical error statistics for each retrieval product, comprising bias profiles, standard deviation profiles and correlation functions, are presented and discussed. One practical result of the study is the specification of simple analytical observation error covariance matrices for refractivity, which is described in section 6, where also the applicability to other parameters beyond refractivity is discussed. Section 7 finally summarizes the findings and conclusions of the study and provides a brief outlook to further investigations.

2. Ensemble Design and Simulations

[10] The simulation of the data ensemble, from occultation event simulations via excess phases to atmospheric retrieval products, was performed with the End-to-end GNSS Occultation Performance Simulator (EGOPS) [*Kirchengast et al.*, 2002]. Quasi-realistic atmospheric and ionospheric models as well as realistic error characteristics

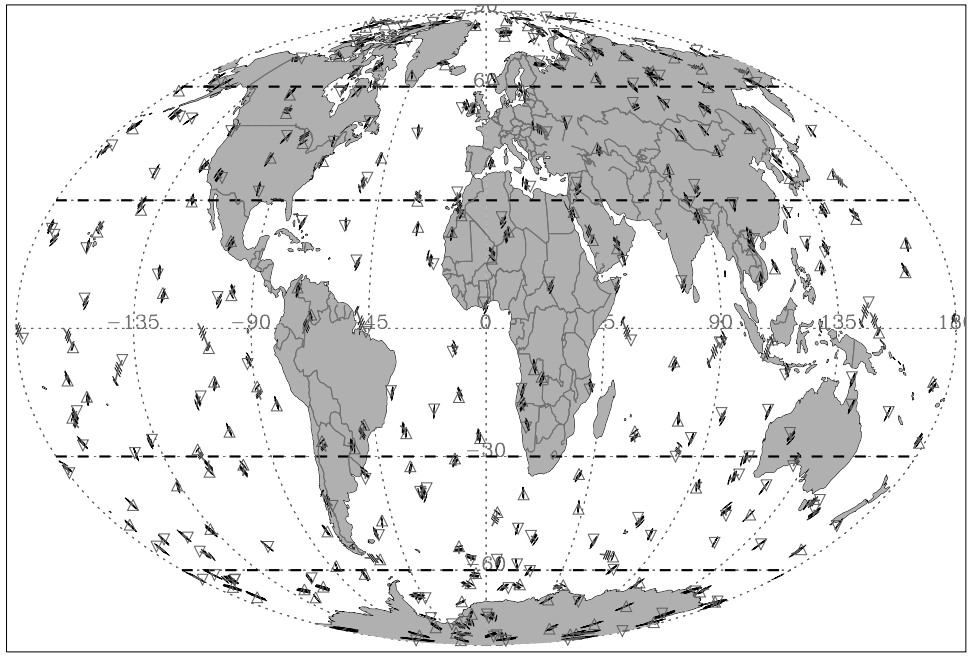

Figure 1. Distribution of the 300 occultation events used in the study; rising occultations (triangles), setting occultations (upside-down triangles), latitude circles delimiting selected latitude bands (heavy dashed lines). For each individual event (inspect, e.g., the event at the equator at about −110 deg longitude as a clear example), small lines give an indication of the "verticality" of the event (the shorter the tangent point trajectory/heavy line, the more vertical) and of the occultation plane orientation (orientation of the parallel light solid lines), respectively.

were involved in order to obtain reliable simulated occultation data.

[11] Occultation events were simulated for one day, September 15, 1999, adopting the planned European Meteorological Operational satellite (METOP) [*Edwards and Pawlak*, 2000] as Low Earth Orbit (LEO) satellite and its GNSS Receiver for Atmospheric Sounding (GRAS) [*ESA/EUMETSAT*, 1998; *Silvestrin et al.*, 2000] as sensor. Rising and setting occultation events were taken into account employing the GPS satellites as transmitter system. The number of simulated events for this day was 574 in total. In order to save computation time with respect to the time consuming forward modeling, we chose an ensemble of 300 occultation events equally distributed in space and time with 100 events in each of three latitude bands, low (−30° to +30°), middle (±30° to ±60°), and high (±60° to ±90°) latitudes. Figure 1 illustrates the distribution of these 300 profiles, which were used for the following simulations and error analysis.

[12] The atmospheric modeling was based on an ECMWF operational analysis field (Sept. 15, 1999, 12 UT) used as reference atmospheric state for the simulations, with resolution T213L50 (operational resolution at ECMWF in Sept. 1999, ∼60 km × 60 km horizontal grid spacing, 50 vertical levels up to 0.1 hPa, i.e., ∼65 km height). This horizontal sampling of the model field is about 5 times higher than the along-ray horizontal resolution of RO data of about 300 km [e.g., *Kursinski et al.*, 1997] and is capable of representing weather features such as frontal systems, but smaller scale horizontal variations are no longer resolved. Figure 2 shows exemplary slices of temperature and specific humidity, extracted from the ECMWF operational analysis field, which indicate the reasonably realistic nature of the model for the purpose of the study. Proper computation of the atmospheric variables of interest (refractivity, temperature, etc.) at arbitrary locations within the gridded ECMWF field, as needed for this study, is part of the EGOPS atmospheric models software [*Kirchengast et al.*, 2002].

[13] The ionosphere was prescribed with the NeUoG model, which is a global empirical solar-activity and local-time dependent 3D climatological model of the ionospheric electron density field developed by *Leitinger et al.* [1996]; a moderate solar activity index $F_{10.7} = 130$ was supplied to the model for the present study. The model does not account for small scale irregularities, which has to be taken into account when interpreting the results of this study. NeUoG was of good use already in other occultation-related studies [e.g., *Leitinger and Kirchengast*, 1997; *Steiner et al.*, 2001; *Gobiet and Kirchengast*, 2004].

3. Phase and Doppler Observables

[14] The geometry for each occultation event was calculated based on Keplerian orbits. Based on geometric optics forward modeling of the signal propagation through the atmosphere-ionosphere system was performed with a sub-millimetric precision 3D ray tracer providing signal profiles as seen by the sensor. Since ray tracing stops at multipath situations in the lower troposphere in case of sharp vertical gradients, this study does not include multipath and diffraction effects, which has to be kept in mind

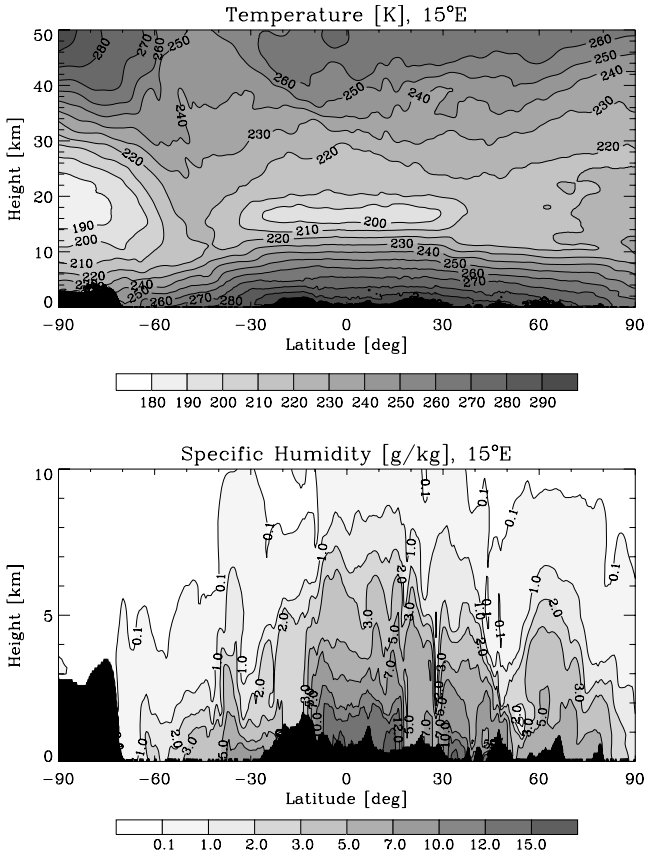

Figure 2. ECMWF T213L50 operational analysis field of September 15, 1999, 12 UT, at 15°E: (top) temperature slice and (bottom) specific humidity slice. See color version of this figure at back of this issue.

when interpreting the results at heights below 5 km in the lower troposphere.

[15] Observation system modeling was subsequently performed to superpose instrumental and raw processing system effects on the forward modeled signal. The results are fairly realistic excess phase path profiles reflecting the GRAS receiving system performance [*Silvestrin et al.*, 2000; *Ramsauer and Kirchengast*, 2001]. Modeling of the observation system error characteristics comprises precise orbit determination (POD) errors, antenna pattern, local multipath, receiver thermal noise, and clock instabilities. The POD error model contains satellite positioning and velocity errors with the along-ray velocity error of 0.05 mm/s being the dominant error source. The radial position errors of the GPS and the LEO satellites were fixed at 0.2 m and at 0.4 m, respectively, a conservative bound for modern POD performance. Receiver noise was modeled as white Gaussian noise for a LEO antennae noise temperature of 150 K and a loop bandwidth (single-side) of 10 Hz. Local multipath effects were modeled using a sinusoidal shaped function with the multipath phase error amplitude set to 0.5 mm and the multipath phase error period set to 100 sec. The modeling of clock errors, representative of the performance of high-quality ultra-stable oscillators (USOs), was based on a random walk model and a ground-based single-differencing clock correction method with the relative stability of the ground clock set to a 1-sec Allan deviation of 1×10^{-13}. *Ramsauer and Kirchengast* [2001] performed a thorough error budget analysis for a GRAS-type receiving system and more details can be found therein.

[16] Figure 3 (left column) shows the ionosphere-corrected excess phase path LC for the global ensemble (Figure 3a) and for the three latitudinal data sets (Figures 3b–3d), with the mean LC excess phase path indicated for the latitudinal data. An occultation event starting/ending at 90 km (0 sec) lasts 1–2 min with a (neutral-gas) excess phase path of about 2 mm near the mesopause (~80 km/~4 sec; in Figure 3, left column, involving ionospheric residuals), ~20 cm near the stratopause (~50 km/~16 sec), and >20 m below the tropopause level (~15 km/~30 sec). The near surface excess phase path reaches ~0.7–2 km depending on the water vapor content of the atmosphere. The ionospheric residual after linear ionospheric correction of phases is of the order of a few centimeters, which can be seen in the phase path profiles in the first few seconds of the occultation, especially in the mean profiles of the ensembles. The different latitudinal ensembles reflect the varying influence of the ionosphere, showing ionospheric residuals of up to ~1 cm at high latitudes increasing to up to ~10 cm at low latitudes. Since the ionospheric model used does not account for small-scale ionospheric noise (see section 2), this noise component which can act to increase random noise on top of thermal noise and clock noise is not represented in the present end-to-end simulations. Dependent on ionospheric conditions, real RO data may thus exhibit somewhat increased random noise, which needs careful filtering in the processing of real data [e.g., *Gorbunov*, 2002].

[17] Figure 3, furthermore, illustrates the phase errors (middle column) and associated Doppler errors (right column), which are shown without the ionospheric errors in order to explicitly depict the errors due to the GRAS receiving system specifications. The error statistics for the LC phase is based on difference profiles each of which was computed by subtracting the raw phase profile without observational error from the phase profile including observational error. Calculation of the mean of the difference profiles led to the bias profile. Furthermore, profiles of the standard deviation and of root mean square (rms) error were calculated (the latter not shown in Figure 3, since essentially identical with the standard deviation). Relative error quantities (percentage errors) were derived by relating the absolute error quantities to the mean phase profile (Figure 3, left column) and by multiplying it with the factor 100. The errors in the Doppler shift, the time derivative of the phase (see section 4 below), were computed in the same manner.

[18] The standard deviation (and also the rms error, since the bias contribution is negligible) of the LC phase sampled at 10 Hz is found to be 2–3 mm at <30 sec (above the tropopause), which reasonably reflects the METOP/GRAS receiving system performance [*Silvestrin et al.*, 2000]. While absolute errors increase into the troposphere to 25 mm, the relative standard deviation is found to be <0.02% at these low heights. The Doppler shift exhibits a standard deviation and rms of ~3 mm/sec above the tropopause. Also for the Doppler shift, relative errors are found <0.02% in the troposphere. Biases in both, excess

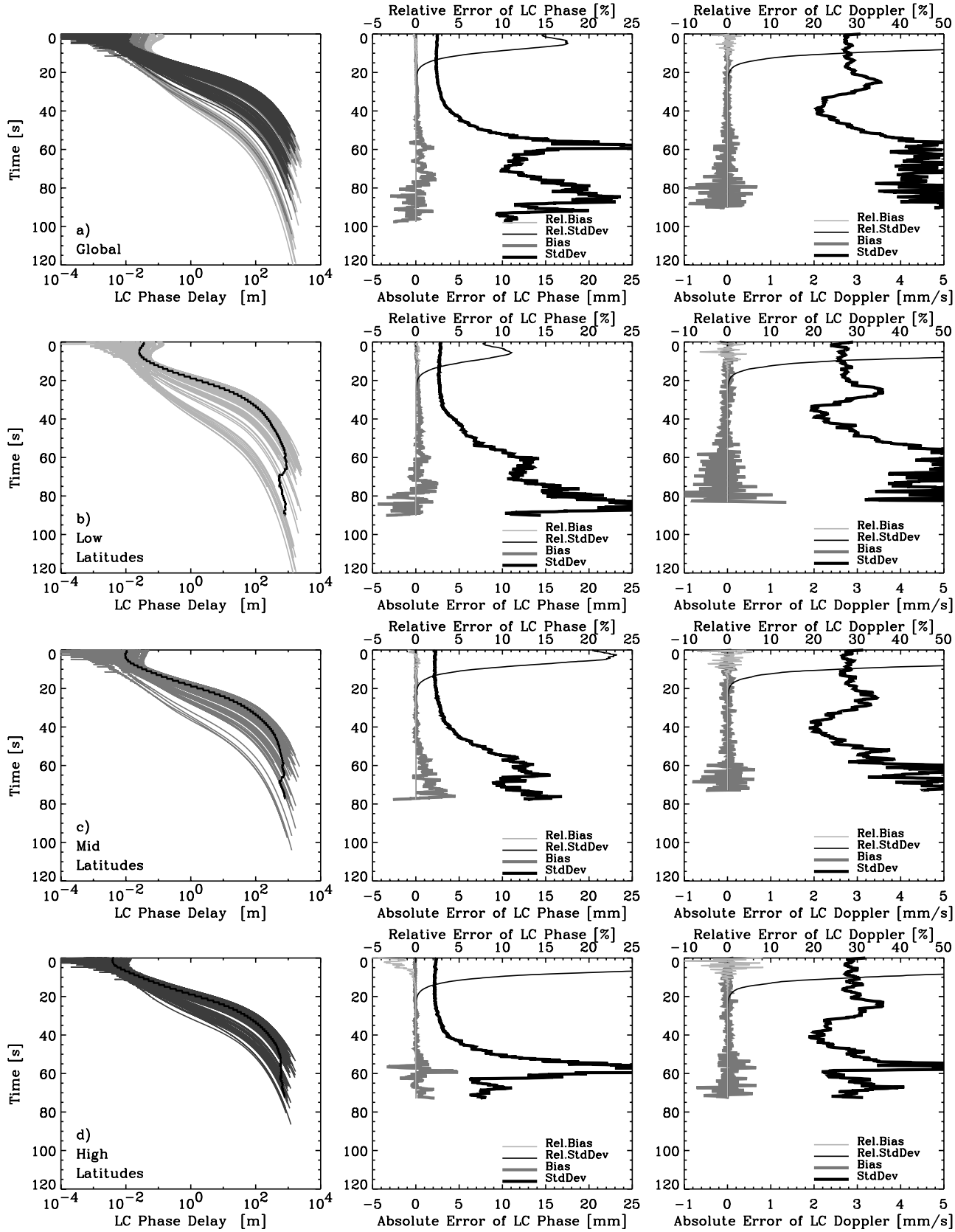

Figure 3. The left panels show the ionosphere corrected LC excess phase path for the global ensemble (a) and the latitudinal ensembles (b–d); for the latter three also the mean profile of each ensemble is shown (heavy black line). The middle and right panels show the associated absolute (heavy) and relative (light) bias (grey) and standard deviation (black) of the LC phase delay (middle) and Doppler shift (right), respectively.

phase and Doppler shift, are negligible, reflecting the self-calibrated nature of these basic observables.

4. Retrieval of Atmospheric Profiles

[19] The calculation of atmospheric profiles from excess phase paths included filtering of the phases with a regularization method resembling a low pass filter to eliminate high frequency noise [*Syndergaard*, 1999]. Time-derivation of the filtered phase path data led to the Doppler shift, from which bending angles were calculated. We applied the ionospheric correction of bending angles, which leads to a considerably smaller residual bias in derived bending angles than the phase correction method [*Vorob'ev and Krasil'nikova*, 1994; *Hocke et al.*, 1997].

[20] The processing involved an initialization of retrieved bending angles with background bending angles derived from the MSISE-90 climatology [*Hedin*, 1991]. A background search in the height interval of 40–55 km was performed to find the best-fit background bending angle profile by using a least squares criterion. An inverse-covariance-weighting statistical optimization [*Healy*, 2001a] was applied to combine observed and background bending angle profiles as described in detail by *Gobiet and Kirchengast* [2004].

[21] Briefly, for the specification of the background error covariance matrix a relative standard deviation of 20% of the background bending angle was assumed, and the variances constituting the diagonal elements of the covariance matrix set accordingly. The off-diagonal elements representing covariances were calculated by assuming an exponential correlation decay with a correlation length of 6 km, representing the length scale at which the inter-level correlation is decayed to 1/e. The observation error was estimated as the standard deviation of the observed bending angle profile from the background profile between 70 and 80 km, where the bending angle signal is small and ionospheric residual and measurement noise dominate. The average standard error of the 300 retrieved bending angles was found to be $\sim$1.2 μrad, fairly consistent with the accuracy requirement specification of 1 μrad of the METOP/GRAS operational RO receiving system [*ESA/EUMETSAT*, 1998]. For reference and scaling, bending angle accuracy from present experimental RO systems such as CHAMP/GPS is found more at the 2–3 μrad level (A. Gobiet, University of Graz, Austria, private communications, 2004). The off-diagonal observation error covariance elements were set to follow an exponential decay with a correlation length of 1 km. All these settings are based on fairly extensive adequacy and sensitivity tests, partly inherited from earlier studies and related development work [*Sokolovskiy and Hunt*, 1996; *Hocke et al.*, 1997; *Healy*, 2001a; *Steiner et al.*, 2001].

[22] Refractivity, pressure, geopotential height, temperature, and specific humidity profiles were calculated from the bending angle profiles by using, from bending angle via refractivity towards dry temperature, a classical GPS RO retrieval chain summarized by *Gobiet and Kirchengast* [2004]. A detailed review of the algorithms involved was given by *Kursinski et al.* [1997]. In the troposphere, an optimal estimation temperature and humidity retrieval algorithm was applied to refractivity, using the ECMWF 24-hour short-range forecast valid at September 15, 1999, 12 UT (the time of the model analysis field used for the present simulations) as background field for temperature and humidity. This algorithm is an implementation closely following the variational retrieval (1D-Var) algorithm of *Healy and Eyre* [2000]. It was implemented for a latitude-dependent tropospheric top height defined to decrease linearly with latitude from 15 km at the equator to 9 km at the poles. Down to this height ($z \geq z_{\mathrm{top}}$), standard dry air retrieval was applied, with a smooth half-Gaussian weighted transition (i.e., weighting $\exp[-(|z - z_{\mathrm{top}}|/\Delta z)^2]$) to the 1D-Var solution over a width scale of 2 km (Δz) below this height ($z < z_{\mathrm{top}}$).

[23] For the background error, covariance matrices following an exponential decay with a correlation length of 3 km for temperature and specific humidity were adopted. The standard deviation of the background specific humidity was assumed 20% at 0 km linearly increasing to 50% at 10 km and kept constant further up. The standard deviation of the background temperature was taken constant with height but dependent on latitude with 1.5 K at high, 1.25 K at middle, and 1 K at low latitudes, respectively. These simple settings were checked by comparing the background with the true profiles and by comparing to the specifications given by [*Andersson et al.*, 2000]. They were found to reasonably reflect the uncertainty of the short-term forecast fields used as background; limited further improvement may be achieved by using more sophisticated forecast error covariance matrices [e.g., *Derber and Bouttier*, 1999]. The refractivity error covariance matrix was specified following an exponential decay with a correlation length of 2 km, and a latitude and height dependent standard deviation. The standard deviation of refractivity was 0.8%, 1.4%, 2% at 0 km linearly decreasing to 0.2%, 0.2%, 0.1% at 10 km and staying constant further up for high, middle, and low latitudes, respectively. These settings were based on the refractivity error analysis results of this study itself.

5. Analysis Results and Discussion

[24] For each atmospheric retrieval product an empirical error analysis was performed as follows. We computed, for each retrieved profile, the co-located ECMWF analysis vertical profile at the mean tangent point location of the event to serve as the "true" profile. Based on the difference profiles of the retrieved profiles and the "true" profiles we calculated sample mean deviations (bias profiles) as well as sample error covariance matrices including sample standard deviation profiles and sample error correlation matrices, respectively. Relative error quantities were obtained by dividing the absolute ones by the mean profile of the "true" profiles and multiplying this ratio with 100.

[25] For each ensemble, we computed these statistical estimators with the usual expressions [e.g., *Anderson*, 1984; *Steiner and Kirchengast*, 2004] at a standard vertical grid with 60 levels chosen to correspond to an ECMWF L60 grid (available from http://www.ecmwf.int/products/data/technical/model_levels/model_def_60.html), which is the present vertical grid of ECMWF operational analyses. Using the L60 hybrid pressure levels definition, 60 standard pressure levels were computed using a standard surface pressure of 1013.25 hPa. From these 60 pressure levels, the standard

height levels used throughout were obtained with the barometric height formula using a standard scale height of 7 km. This type of vertical grid for computing the statistics was chosen since it provides the error analysis results at a vertical sampling closely consistent with that of a modern numerical weather prediction system such as ECMWF's.

[26] The error estimates include both the observational error (due to the measurement and retrieval process) and the representativeness error (due to atmospheric horizontal variability), the latter becoming important in the lower troposphere due to increased horizontal variations [*Foelsche and Kirchengast*, 2004b; *Syndergaard et al.*, 2004]. The representativeness error depends on the resolution of the model data used for the simulations. Low resolution data sets do not resolve horizontal gradients well, resulting in smaller errors as shown by *Zou et al.* [2002], while the effects of horizontal gradients in meso-scale simulations produce larger errors [*Healy*, 2001b]. The restrictions of the present study are that small scale structures are not resolved by the input models (see section 2 for model resolution and section 3 for discussion of ionospheric residual errors) and that possible seasonal dependencies of RO errors [*Marquardt et al.*, 2001] are not represented since a single-day data set is used. These potential additional error contributions have to be kept in mind when interpreting the results. Figures 4–9 present the error analysis results of each retrieval product from bending angle, via refractivity, pressure, geopotential height, to temperature and specific humidity.

[27] The results are shown for the global ensemble (panel row a) and for the latitudinal data sets (panel rows b–d) up to 50 km height. The left panels show the number of events entering the error statistics at a given height. The middle panels illustrate the error characteristics in terms of absolute and/or relative quantities of bias and standard deviation profiles. For visual clarity we did not draw statistical significance bounds for the bias profiles but note that the standard deviation of bias at each height is the standard deviation divided by the square-root of the number of events in the ensemble (left panel). For example, for 100 events the 2-sigma uncertainty of the bias is thus 5 times smaller than the standard deviation implying that, e.g., the bending angle and refractivity profiles are found generally unbiased all over the domain.

[28] We refer primarily to relative error quantities for the atmospheric parameters with near-exponential height decrease and to absolute error quantities for geopotential height and temperature. These primarily-referred-to error quantities are denoted by heavy lines, solid black for the standard deviation and solid grey for the bias, respectively. Mean atmospheric profiles are depicted by light dotted grey lines. The right panels display error correlation functions, which are defined as the rows of the error correlation matrix. They are displayed for three different height levels ($\sim$40 km, $\sim$20 km, $\sim$5 km) representative of upper stratosphere, lower stratosphere, and troposphere. For humidity, three representative tropospheric levels are shown ($\sim$7 km, $\sim$5 km, $\sim$3 km). The error correlation functions express the correlation of errors at these specific heights with the errors in the remainder of the profile.

[29] When interpreting and using the bending angle error results it has to be taken into account that the "true" bending angle was computed here by Abel transform from the "true" refractivity assuming spherical symmetry. While this still leads to reasonable results in the stratosphere and upper troposphere it does not represent with full adequacy the errors under significant horizontal variations below $\sim$7 km [*Foelsche and Kirchengast*, 2004b].

[30] Bending angle: Figure 4 displays the error statistics for the bending angle profiles showing the mean bending angle profile to range from $\sim$20 mrad at near 2 km to $\sim$15 μrad at 50 km impact height. The global data set shows a relative bias of the bending angle of <0.1% at 5–40 km with a maximum of 0.5% outside this height interval. The 0.1% bias height interval shrinks to $\sim$7–30 km at mid latitudes. Maximum bias values of up to 1% occur below 5 km impact height at all latitudes. The relative standard deviation (Rel.StdDev) of the bending angle is 0.2–1% between $\sim$8–35 km, increasing to about 5% at 50 km at all latitudes. In the troposphere, the Rel.StdDev increases to $\sim$5% at high latitudes and to $\sim$8% at low and mid latitudes.

[31] Comparison of these empirical bending angle errors with the findings in theoretical studies [*Syndergaard*, 1999; *Rieder and Kirchengast*, 2001b] shows that the theoretical estimates of the standard deviation appear somewhat smaller than the empirical ones. *Rieder and Kirchengast* [2001b] report a Rel.StdDev of <1% below $\sim$37 km for a standard receiver scenario (SR; GPS/MET receiver type) and below $\sim$43 km for an advanced receiver scenario (AR; GRAS receiver type) while our results shows a 1%-height at 35 km. The difference can be explained by the set up of the theoretical study: a lower vertical resolution was used leading to higher accuracy ($\sim$4 km resolution near the stratopause instead of $\sim$2 km here), no ionospheric errors, assumption of lower background bending angle uncertainty ($\sim$10% near the stratopause instead of 20% here) and higher excess phase accuracy (2 mm instead of $\sim$2.5 mm here). Accounting for the differences, the stratospheric results of that theoretical error analysis are found consistent with the present empirical analysis results. Since our study involves significantly less restrictive assumptions (no linearity, unbiasedness, dry air, and spherical atmosphere assumptions), the results obtained here are more realistic. Still it is to be kept in mind that data products from different measurement and retrieval processes than here (i.e., other than GRAS-type receiving system performance, different retrieval algorithms) will need at least a scaling of the present results to those different conditions, if not repeat of the error analysis itself, in case of severe differences.

[32] Deriving from uncorrelated measurements of excess phase time series, the bending angle errors are uncorrelated except for small negative correlations of the given height levels with their lower and upper neighboring levels. These negative correlations stem from derivative operations at the step from phase to Doppler shift [*Syndergaard*, 1999; *Rieder and Kirchengast*, 2001b] and are most pronounced in the low latitude ensemble at lower to middle stratospheric heights where they reach values of about -0.4.

[33] Refractivity: Figure 5 displays the error statistics for the refractivity profiles with the mean refractivity profile ranging from $\sim$280 [N units] at 1 km to $\sim$0.2 at 50 km height. Refractivity exhibits a Rel.StdDev of 0.1–0.75% and a relative bias of <0.1% at 5–40 km height in all data sets. Outside this "core" domain, the relative bias reaches

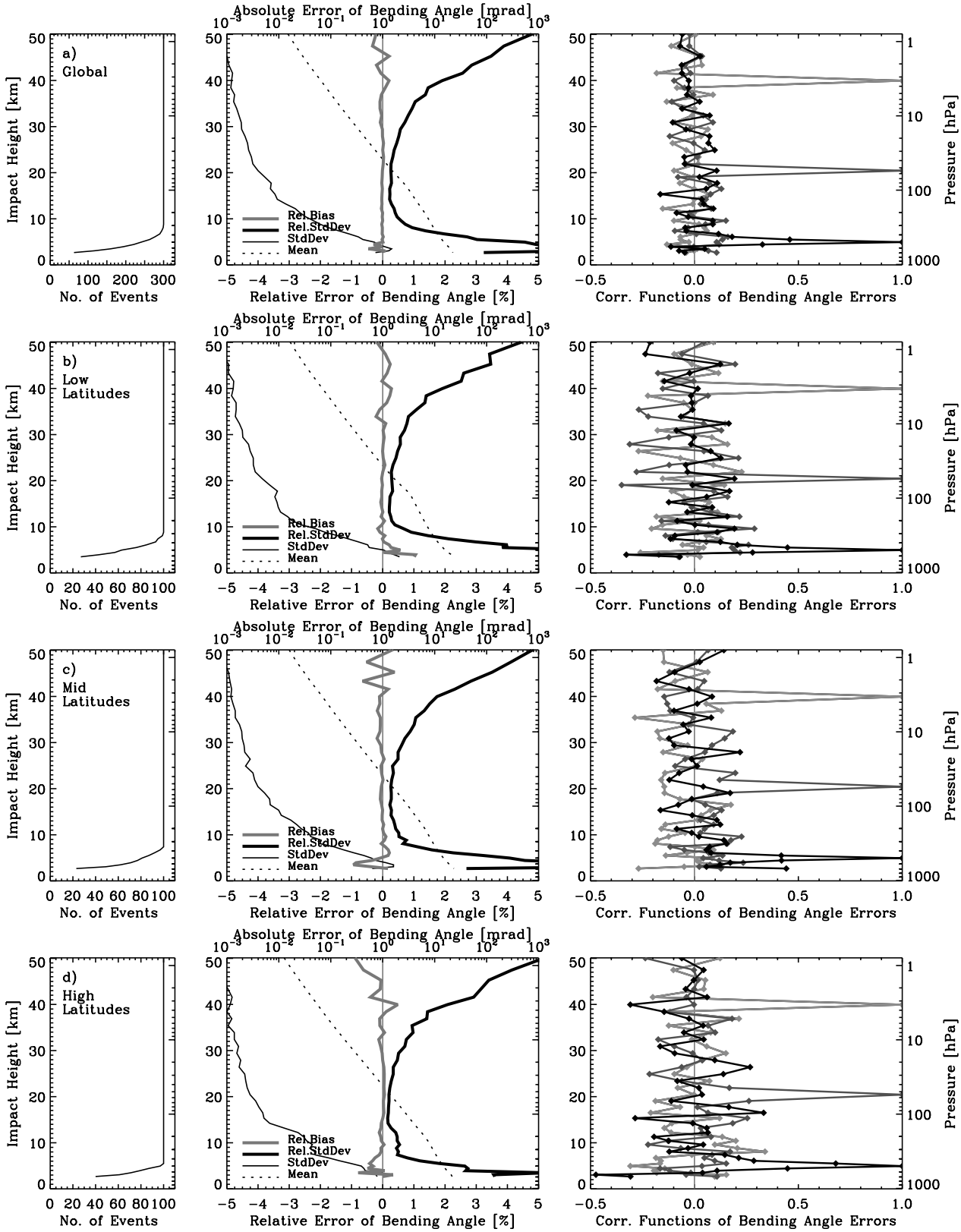

Figure 4. Bending angle error analysis results, as a function of impact height, for the global (a) and the latitudinal (b–d) ensembles. (left) Number of events used for the error statistics calculation at any given height. (middle) Relative bias (heavy grey), relative standard deviation (heavy black) as well as the absolute standard deviation (light black) and the mean of the "true" profiles (dotted). (right) Error correlation functions for ~40 km (light grey), ~20 km (dark grey), and ~5 km (black) height, representative of upper stratosphere, lower stratosphere, and troposphere, respectively.

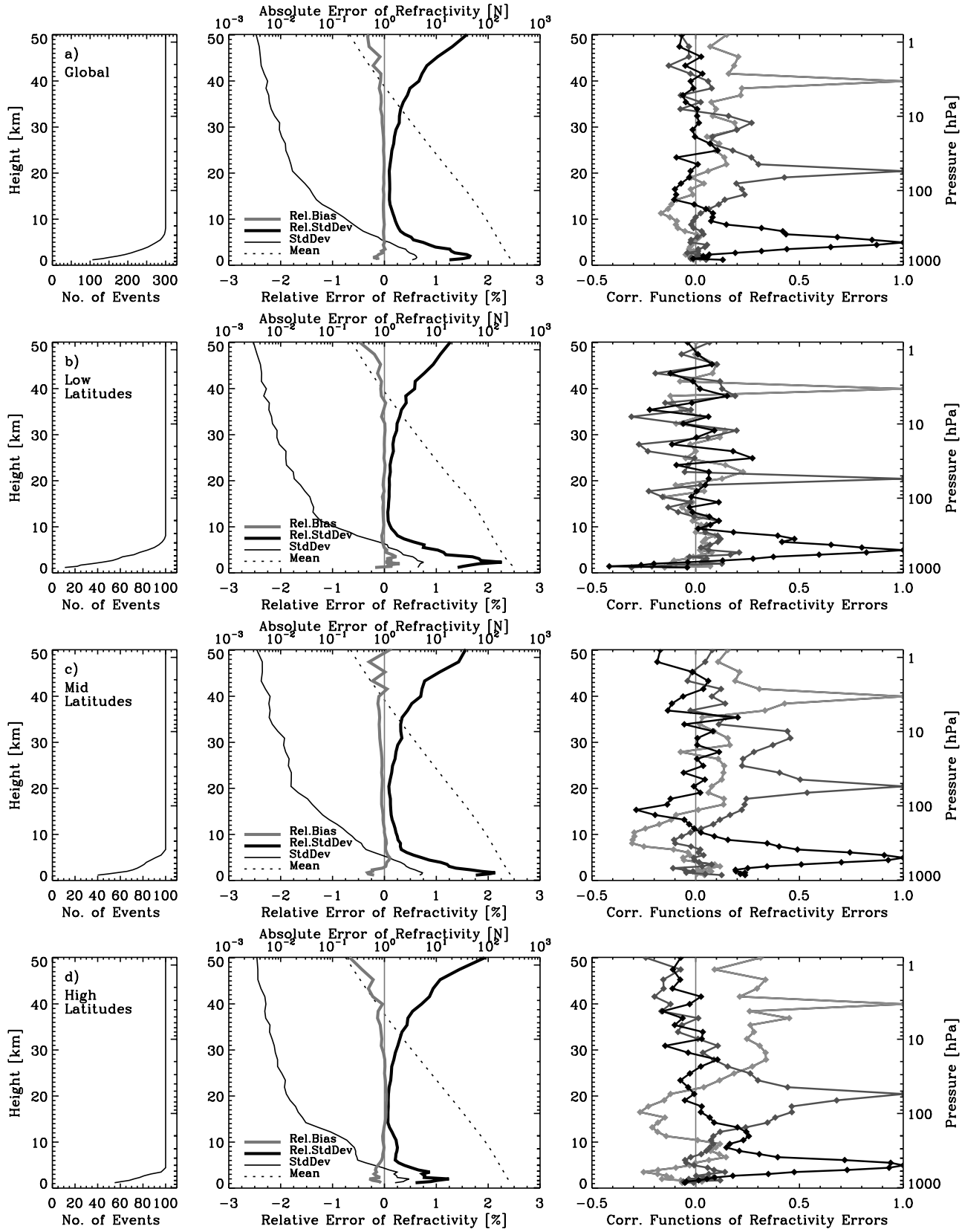

Figure 5. Refractivity error analysis results, as a function of height, for the global (a) and the latitudinal (b–d) ensembles. Figure layout and style same as Figure 4; see that caption for details.

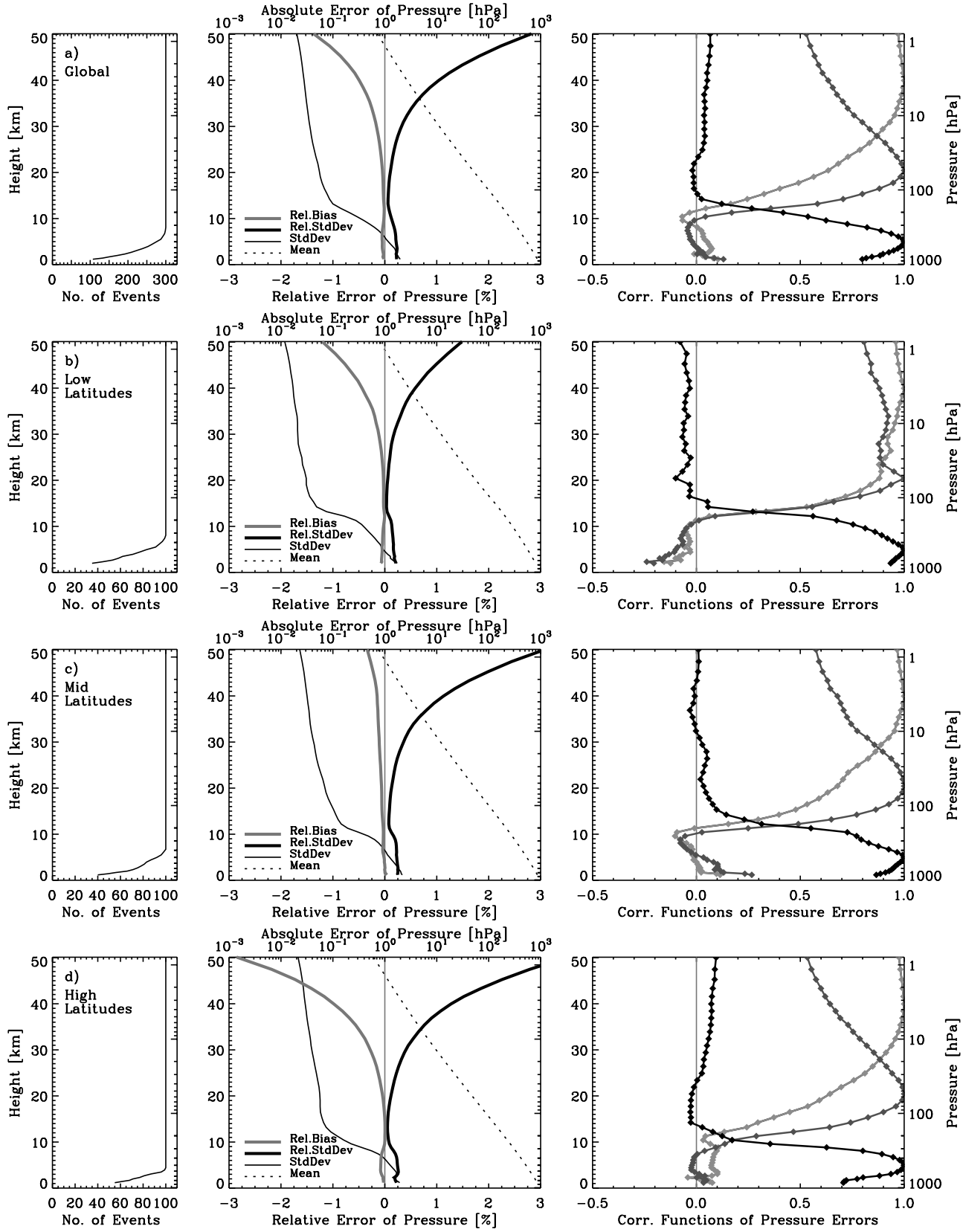

Figure 6. Pressure error analysis results, as a function of height, for the global (a) and the latitudinal (b–d) ensembles. Figure layout and style same as Figure 4; see that caption for details.

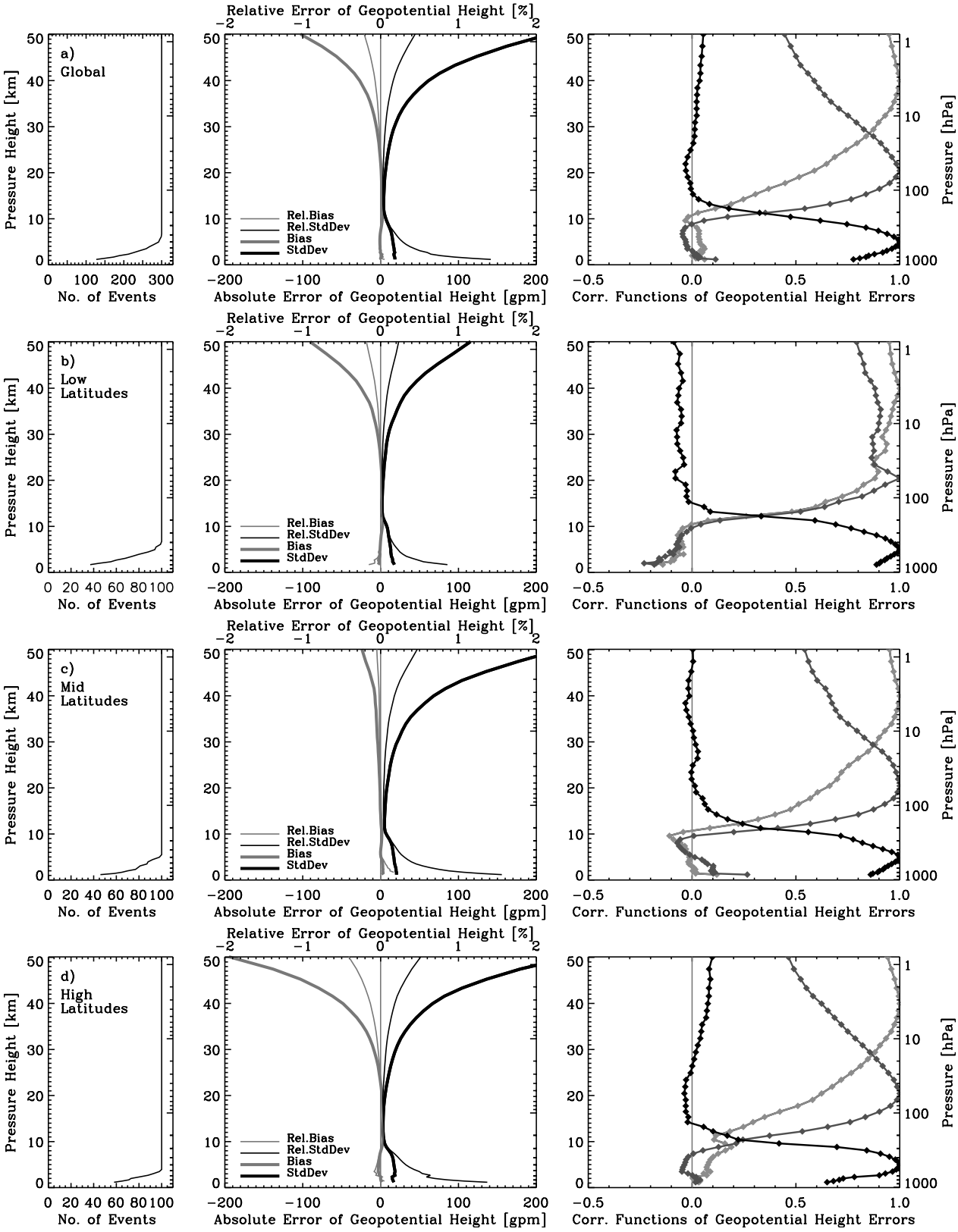

Figure 7. Geopotential height error analysis results, as a function of pressure height, for the global (a) and the latitudinal (b–d) ensembles. (left) Number of events used for the error statistics calculation at any given height. (middle) Absolute bias (heavy grey), absolute standard deviation (heavy black) as well as relative bias (light grey) and relative standard deviation (light black). (right) Error correlation functions for ~40 km (light grey), ~20 km (dark grey), and ~5 km (black), representative of upper stratosphere, lower stratosphere, and troposphere, respectively.

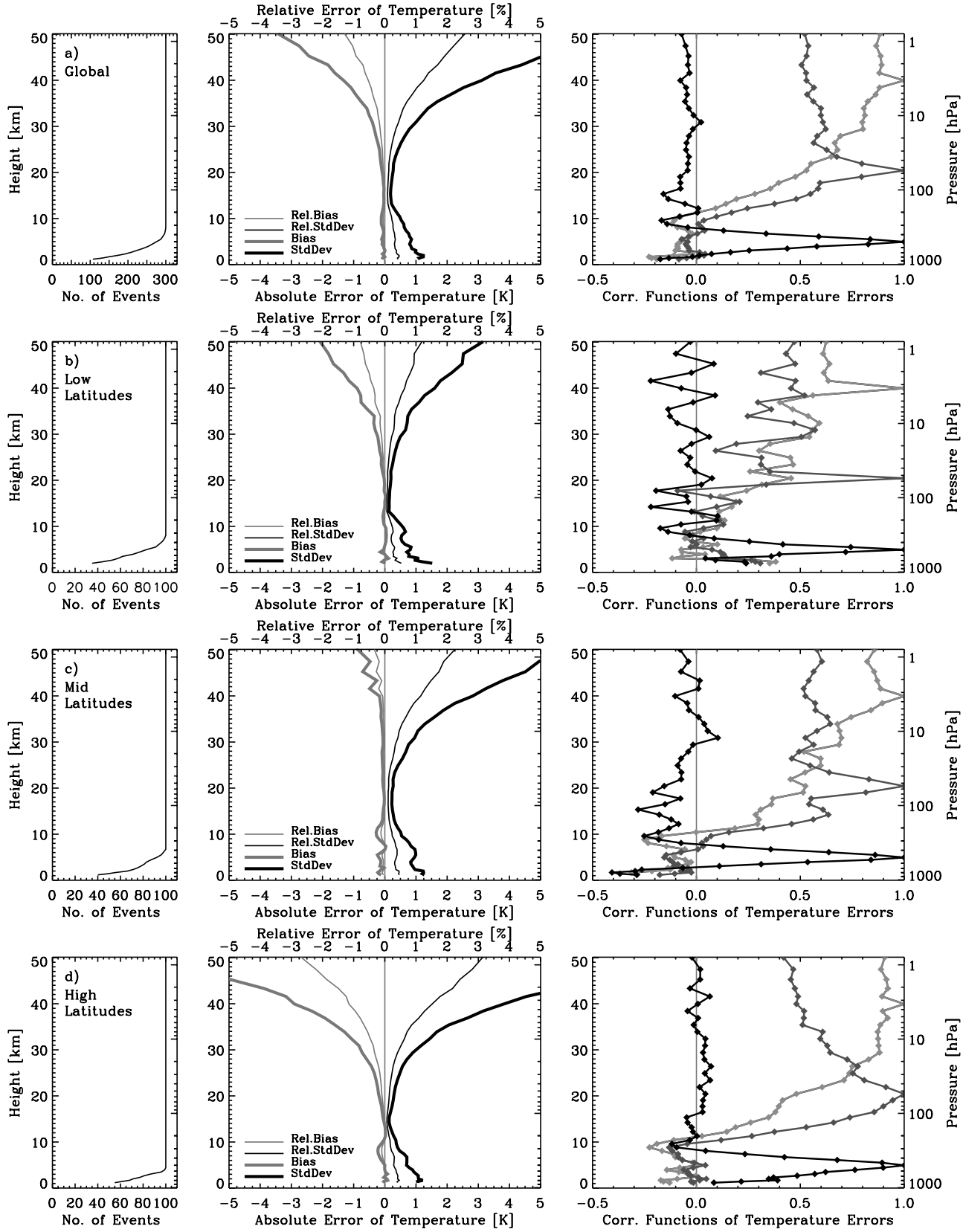

Figure 8. Temperature error analysis results, as a function of height, for the global (a) and the latitudinal (b–d) ensembles. Figure layout and style same as Figure 7; see that caption for details.

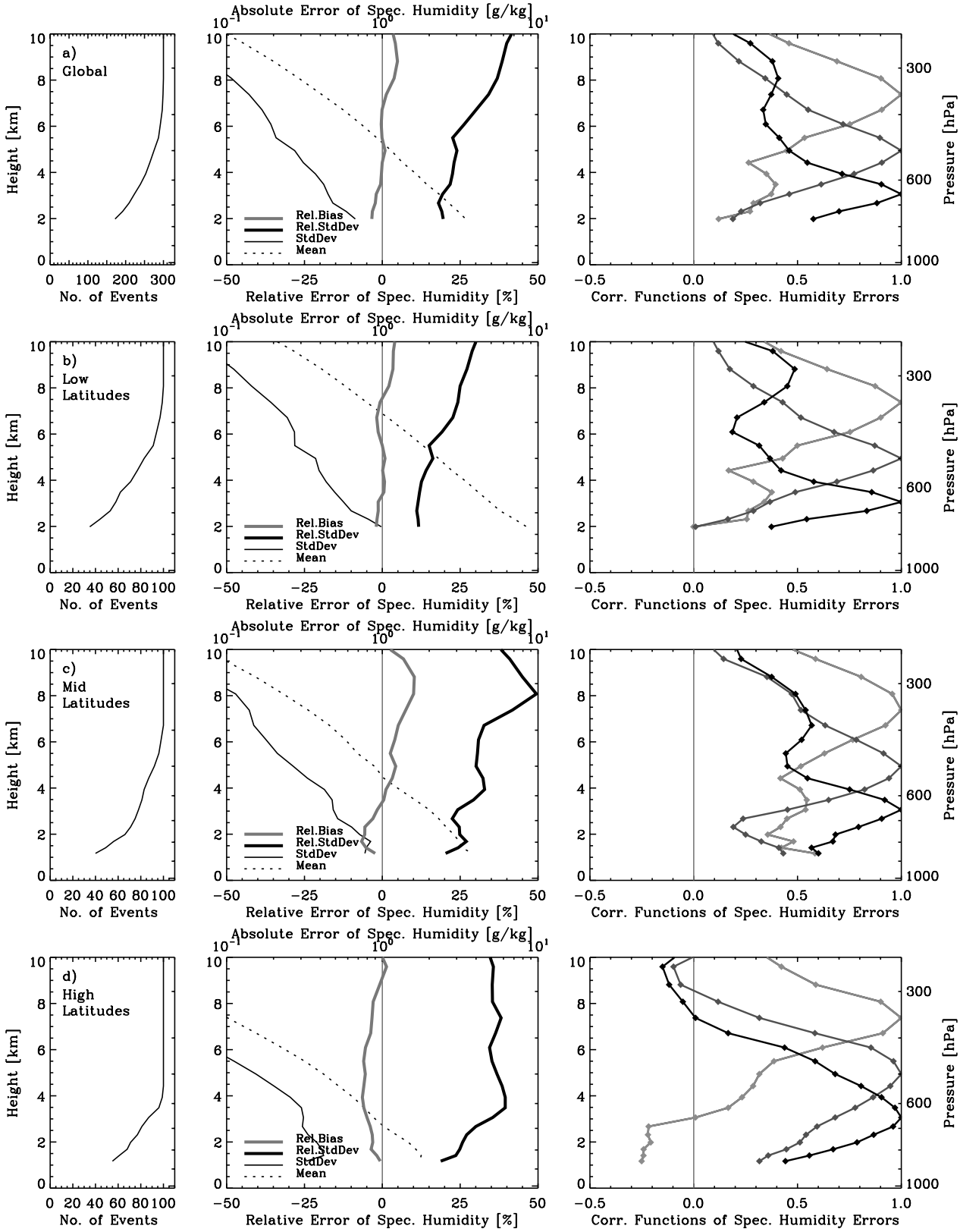

Figure 9. Specific humidity error analysis results, as a function of height, for the global (a) and the latitudinal (b–d) ensembles. (left) Number of events used for the error statistics calculation at any given height. (middle) Relative bias (heavy grey), relative standard deviation (heavy black), as well as the absolute standard deviation (light black) and the mean of the "true" profiles (dotted). (right) Error correlation functions for tropospheric height levels at ~7 km (light grey), ~5 km (dark grey), and ~3 km (black) height.

0.3% in the lower troposphere at all latitudes and up to 0.7% at 50 km height at high latitudes. The relative standard deviation stays below 2% outside the "core" domain, except for the low latitude ensemble, where it reaches ~2.3% at the bottom [*Steiner and Kirchengast*, 2004].

[34] In the *Rieder and Kirchengast* [2001b] analysis, the upper height limit for a Rel.StdDev of <1% is 43 km for the SR scenario and 49 km for the AR scenario, respectively. Our empirically estimated height limit lies in between these heights at 45 km. *Kursinski et al.* [1997] estimated an rms error of refractivity of <0.4% between 5–30/40 km for a bad/good scenario. This agrees well with the empirically derived Rel.StdDev of <0.4% at ~6–36 km height, but at lower tropospheric heights the error derived here is bigger, mainly due to subsuming more horizontal variability error. Our findings are also consistent with the results of a study carried out by *Kuo et al.* [2004], who performed an error analysis of CHAMP and SAC-C data and found the observation error of refractivity to be of the order of 0.3–0.5% at 5–25 km increasing to 3% in the tropical lower troposphere.

[35] The refractivity error correlation functions are broader than the bending angle error correlation functions revealing the effect of the Abelian integration. The broadening in the troposphere seen in the refractivity error correlation functions is mostly a result of the errors due to horizontal variations; it is particularly marked in the mid and high latitude ensembles with negative correlations vanished. Negative correlations are most pronounced in the low latitude ensemble at lower to middle stratospheric heights. Since the error statistics is performed on an L60 height grid, these anti-correlation features are smoothed and can hardly be seen in Figure 5 but can be resolved on a finer grid (further addressed in section 6 below).

[36] As refractivity is the RO data product perhaps most convenient for data assimilation [e.g., *Healy and Eyre*, 2000; *Syndergaard et al.*, 2004], we present in section 6 a simple analytical formulation for refractivity error covariance matrices based on the empirical results obtained.

[37] Pressure: Figure 6 presents the error statistics of pressure with the mean profile ranging from ~900 hPa at 1 km to ~0.7 hPa at 50 km height. For all data sets the Rel.StdDev of pressure is 0.25% in the troposphere decreasing to 0.1% above the tropopause and increasing to 1% at 40 km height.

[38] The relative bias is <0.2% below 30 km and <0.5% below 40 km for the global and low latitude ensembles. The smallest biases occur at mid latitudes, the largest ones at high latitudes, with a relative bias of close to −3% and a Rel.StdDev of ~3% at 50 km. These biases are the result of downward hydrostatic integration of refractivity (or, equivalently, density), which carries residual density biases from above the stratopause, where background information dominates [e.g., *Rieder and Kirchengast*, 2001b; *Gobiet and Kirchengast*, 2004], by about two scale heights downward into the upper stratosphere. This is most readily seen in comparing the high latitude results of Figures 5 and 6 (weaker, but otherwise similar, also in the low latitude results): Inspecting, for example, the height limit of biases smaller than −0.25%, this lies at ~46 km for refractivity (density) (Figure 5d, middle panel) while it lies at ~30 km for pressure (Figure 6d, middle panel). At low latitudes, these heights are ~48 km (refractivity, density) and ~36 km (pressure), respectively. As this type of bias characteristics also maps further into geopotential height and temperature, special efforts are required to keep them as low as possible in magnitude, in order to have the upper stratospheric profiles accurate as high up towards the stratopause as possible.

[39] A common approach at the pressure retrieval is to impose an initialization of the hydrostatic integral, in addition to the initialization at bending angle level. The integration starts at a height between 30 and 50 km initialized by a model temperature usually taken from ECMWF [e.g., *Kursinski et al.*, 1997; *Wickert et al.*, 2004; *Hajj et al.*, 2004]. The most complete discussion of this approach, including sensitivity tests, has so far been given by *Hajj et al.* [2004]. Regarding the climatological use of geopotential heights and temperatures this approach is problematic, since it leads to intricate error characteristics and a priori-dependence in the stratospheric data down to about 20 km, which threats the crucial aims of un-biasedness and a clear understanding of the degree of residual biasedness. For these reasons, we do not perform any "2nd initialization" but use full downward integration of the hydrostatic integral from 120 km. The initialization at 120 km, whether zero or the MSISE-90 pressure as we adopted, has negligible influence on the results below 50 km [e.g., *Steiner et al.*, 1999]. This preferable approach for climatological applications needs fair care in performing the bending angle initialization in order to keep the residual refractivity (density) biases above the stratopause, and consequently the downward-propagated biases in pressure, geopotential height, and temperature, as small as possible (as discussed above and illustrated in Figure 5 versus Figures 6–8, middle panels). *Gobiet and Kirchengast* [2002, 2004] discuss respective optimization algorithm advancements in detail. They report that particularly residual upper stratospheric biases at high latitudes, which are the most salient ones, can be further reduced significantly by bias correction of background bending angle profiles, at least given data of GRAS-type quality (1 μrad bending angle accuracy). *Gobiet et al.* [2004] validated CHAMP RO data with various sources of correlative data in the stratosphere and found that these less accurate current RO data demand initialization with better background bending angle profile libraries than from pure MSIS or CIRA climatologies, e.g., from ECMWF analyses (extended above ~60 km by climatology). Pressure errors, furthermore, exhibit strong correlation due to the hydrostatic integration; see *Rieder and Kirchengast* [2001b] for a theoretical discussion of pressure error correlation properties.

[40] Geopotential height: Figure 7 displays the error statistics of geopotential height, which is discussed with respect to absolute error quantities. The absolute standard deviation of geopotential height is 5–20 gpm below 30 km, staying <70 gpm up to 40 km pressure height for all data ensembles (pressure height $z_p = -(7\ \mathrm{km}) \cdot \ln[p(z)/1013.25\mathrm{hPa}]$, for showing pressure levels as heights). The bias of geopotential height is <5 gpm below 30 km and <30 gpm below 40 km except for the high latitude ensemble. The latter shows a bias of 50 gpm at 40 km, bias and standard deviation increase to 200 gpm at 50 km pressure height. The correlation functions of geopotential height errors are basically the same as for pressure (see right panels of Figures 6 and 7). The same holds for the behavior of relative pressure errors vs. absolute geopotential height

errors (see middle panels of Figures 6 and 7), a property rooted in the physical relation that fractional pressure is proportional to geopotential height.

[41] The results are in good agreement with the findings of *Kursinski et al.* [1997], who published an rms error of ~10 gpm at 10–20 km and with those of *Leroy* [1997] publishing a geopotential height error of <20 gpm at upper tropospheric and lower stratospheric heights.

[42] Temperature: Temperature error is presented in Figure 8 and is also discussed with respect to absolute error quantities. For the global data set, temperature shows a standard deviation of 0.2–1 K at 3–31 km height and a bias of <0.1–0.5 K below 33 km and of <0.1 K below 20 km. In the lower troposphere, the standard deviation does not exceed 1.5 K in all latitude bands; note that it is a result of the 1D-Var retrieval below about 8 km (high latitudes) to 12 km (low latitudes). The temperature bias is lowest at mid latitudes with <0.1–0.2 K at 2–40 km. Large temperature errors occur at high latitudes, revealing a bias of >3 K and a standard deviation of >5 K above 40 km, which is dominating the global error statistics. The reasons for the residual stratospheric biases are the same as discussed above for pressure; the pressure biases transfer to temperature biases via the equation of state for dry air, which expresses that temperature is proportional to pressure divided by refractivity (or density).

[43] The correlation functions of temperature error are reminiscent of both pressure and refractivity correlation. The vertical correlations are most pronounced at high latitudes, least at low latitudes. This indicates that temperature profile errors at high latitudes are more vertically coupled, and hence in particular vulnerable to downward propagation of errors in the retrieval process, in line with the findings based on independent larger-ensemble climatologies (~1000 profiles in total from a full season) of *Steiner et al.* [2001], *Foelsche et al.* [2003], and *Gobiet and Kirchengast* [2004]. The relations determining how both refractivity and pressure errors propagate into temperature errors are somewhat involved and not addressed further here; *Rieder and Kirchengast* [2001a, 2001b] provide some insight. The different shapes of errors and correlation functions below and above the tropopause are due to the application of the 1D-Var retrieval algorithm in the troposphere (see section 4) [*Steiner and Kirchengast*, 2004].

[44] *Kursinski et al.* [1997] found the rms error of temperature to be <1 K at 8/2–30/40 km for a bad/good scenario, which is in good agreement with our empirical estimates of sub-Kelvin accuracy at 3–31 km for the global data set and at 3–36 km for the low latitudes. In fact the error estimates in this study can be viewed in several respects as an advancement and generalization of the *Kursinski et al.* [1997] results under more realistic conditions as possible due to the ensemble-based empirical error analysis approach used here. *Palmer et al.* [2000] applied a 1D-Var retrieval and showed higher temperature errors of 1.5 K below ~30 km and up to 5–8 K at 40–50 km height, mainly due to different assumptions on error covariances.

[45] Specific humidity: The error statistics for specific humidity is presented in Figure 9 and is discussed with respect to relative error quantities again. The global mean profile of specific humidity reaches from ~4–0.1 g/kg at 1–10 km height. In the lower troposphere below 2 km, mean specific humidity exhibits values of ~10 g/kg at low latitudes and of ~2 g/kg at high latitudes, in the upper troposphere near 8 km the mean values range from ~0.6 g/kg at low latitudes to below 0.1 g/kg at high latitudes. Note that all humidity retrieval results are based on the optimal estimation algorithm applied (section 4).

[46] The Rel.StdDev of specific humidity in the global ensemble is 20–25% below 5.5 km increasing to 40% at 10 km height. The low latitude data set reveals a smaller Rel.StdDev of 15–30% at 1–10 km. At mid latitudes the Rel.StdDev increases to 50% at 8 km height, the increase in error above about 7 km indicating the height where the background profile dominates the retrieved profile. At high latitudes, a priori knowledge plays a role already in the lower troposphere in the 1D-Var as used here, since, for example, at 3 km humidity values are smaller than 1 g/kg already and the a priori uncertainty is assumed no more than about 30% at this height. Checking with the background uncertainties shows that the retrieved specific humidity error is everywhere smaller except at high latitudes in the upper troposphere where humidity is low.

[47] An encouraging result from the climatological point of view is the low bias in all humidity data sets: Humidity biases are found smaller or near 5% at all latitudes and heights except at mid latitudes above 6 km, where biases reach up to 10%, despite the quite simplified error covariance specifications used in the optimal estimation (section 4). This finding, together with the small biases also found in temperature below 10 km (Figure 8), indicates that 1D-Var retrieval based on ECMWF short-term forecasts as background can lead to tropospheric humidity and temperature retrievals useful for climatological applications. Our plans for building RO based climatologies consequently include the full range of products from refractivity via geopotential height to temperature and humidity, where the latter parameters will, in the troposphere, be retrieved from refractivity by the optimal estimation approach [*Foelsche et al.*, 2005].

[48] The correlation functions for specific humidity errors are displayed for three tropospheric height levels showing that the statistical errors in humidity are correlated over several kilometers in the troposphere, comparable to the correlation range of refractivity and temperature profiles rather than to that of pressure profiles.

[49] Theoretical estimates by *Kursinski et al.* [1997] on a specific humidity rms error of 10–20% in the lower to middle troposphere are comparable to our empirical estimates in low latitude regions, generally our rms error estimates are more conservative. Good general agreement exists with the results of *Palmer et al.* [2000], who show a 25–35% error at <9 km in specific humidity. Humidity rms errors will always significantly depend on the algorithm used, in particular on the refractivity errors and the error characteristics of the background or other external information used to extract humidity and temperature from refractivity. Optimal estimation is rated the method of choice for this purpose [cf. also *Healy and Eyre*, 2000].

6. Error Covariance Matrices for Refractivity and Other Data Products

[50] Given that refractivity is particularly useful for data assimilation [e.g., *Healy and Eyre*, 2000; *Syndergaard et al.*, 2004], we deduced a simple observation error covari-

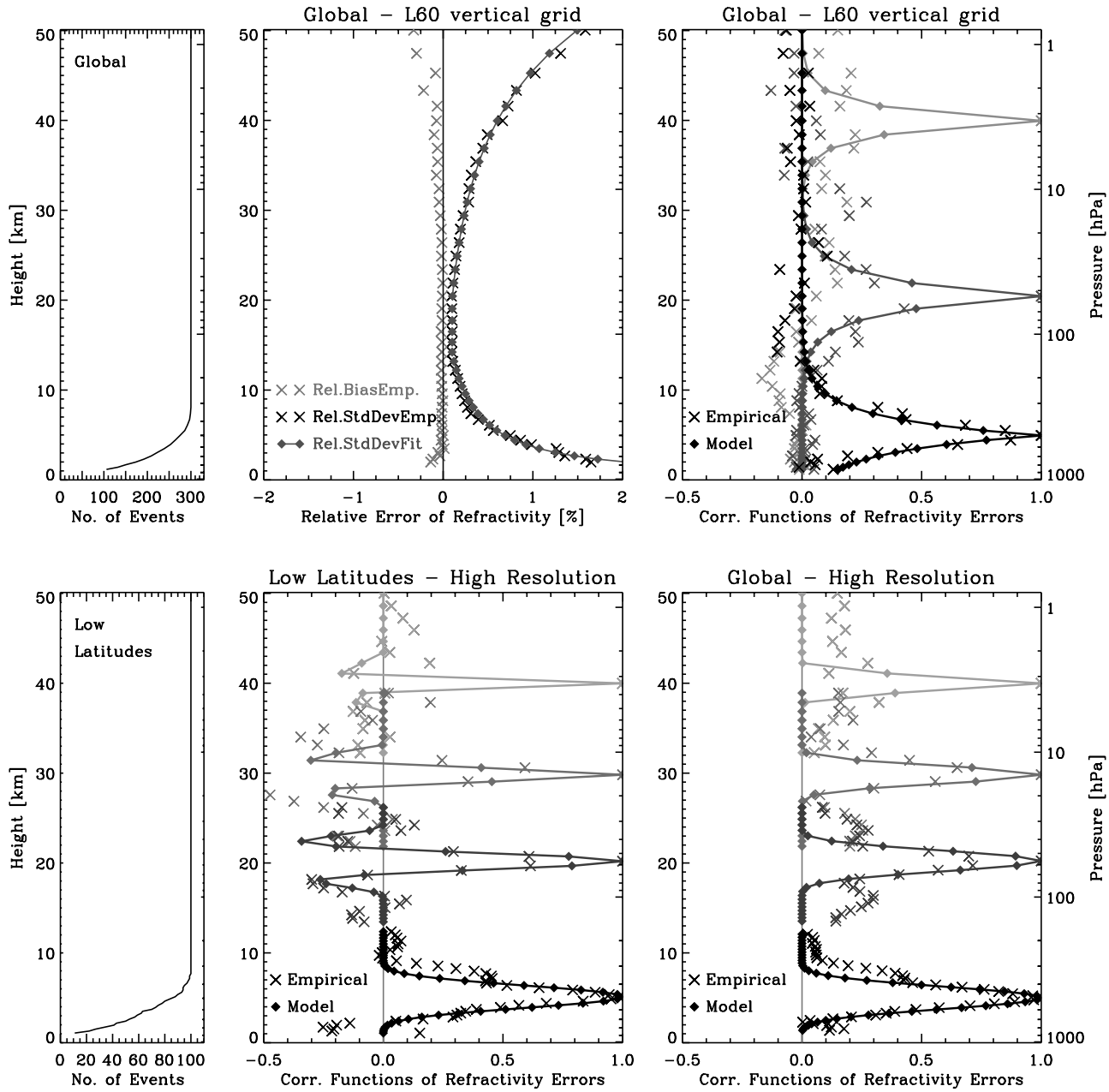

Figure 10. Analytical error models (connected diamonds) fitted to empirical values ("x" symbols) for the specification of refractivity error covariance matrices at an L60-type grid (top panels) and a 90 level grid (bottom panels), respectively. For the standard L60-type grid results for the global ensemble are shown in terms of relative standard deviation (top middle; also bias values indicated as grey "x" symbols) and error correlation functions (top right; for ~40 km, ~20 km, ~5 km height). For the 90 level grid error correlation functions are shown for the low latitude ensemble (bottom middle) and for the global ensemble (bottom right), respectively; the functions shown for ~40 km, ~30 km, ~20 km, and ~5 km height. (left) Number of events used for the error statistics calculation at any given height.

ance matrix formulation for refractivity from the empirical estimation discussed above, for convenient use in data assimilation systems. We performed this in fitting simple analytical functions to the relative standard deviation profile and to the error correlation functions of refractivity. We also comment on the suitability of this model for retrieval products other than refractivity.

[51] We applied a least-squares fit of analytical functions to the empirical relative standard deviation and calculated post-fit residuals of the fit. The functional forms chosen lead to a very small fit residuum (total post-fit residual variance of data against fitted functions within 2–50 km < $(0.15\%)^2$) while conveniently depending on a few parameters only, and exhibit the following simple height dependences. In an upper troposphere/lower stratosphere region between about 14–20 km the relative standard deviation (s) of global refractivity errors is closely constant (value ~0.1%). Above this region it follows an exponential increase (Figure 10,

top; see Figure 5), at least up to the stratopause, which reflects the downward exponential decrease of high altitude initialization errors [e.g., *Kursinski et al.*, 1997; *Rieder and Kirchengast*, 2001b]; more explanation is provided below. From near 14 km downwards, the relative refractivity error is found to increase closely proportional to an inverse-height law. In summary, the standard deviation model $s(z)$ can thus be formulated as

$$s(z) = \begin{cases} s_{utls} + s_0\left[\left(1/z^p\right) - \left(1/z_{troptop}^p\right)\right], & \text{for } 2 \text{ km} < z \le z_{troptop} \quad (1a) \\ s_{utls}, & \text{for } z_{troptop} < z < z_{stratbot} \quad (1b) \\ s_{utls} * \exp[(z - z_{stratbot})/H_{strat}], & \text{for } z_{stratbot} \le z < 50 \text{ km}, \quad (1c) \end{cases}$$

where z denotes the height, $z_{troptop}$ the top level of the "troposphere domain", $z_{stratbot}$ the bottom level of the "stratosphere domain", and s_{utls} the relative (fractional or percentage) error in the "upper troposphere/lower stratosphere domain", respectively. For our global refractivity results, we found $z_{troptop}$ = 14 km and $z_{stratbot}$ = 20 km as best domain boundary heights, and s_{utls} = 0.1% as best-fit constant error between these heights (equation (1b)). This constant height range marks the transition of the exponential error decrease from above and the inverse-height error decrease from below; the fit residual is fairly insensitive to the exact setting of $z_{troptop}$ and $z_{stratbot}$ so that these heights can be safely rounded to full-kilometer values as done here.

[52] Above $z_{stratbot}$, an exponential function was fitted within 20–50 km (equation (1c)), with H_{strat} denoting the scale height of the error increase over the stratosphere. Figure 10, top-middle panel, illustrates this fit. We found a best-fit value of H_{strat} = 11.1 km for the error scale height. The model may also be valid over some height domain beyond the stratopause, the vertical extent of which will depend on the exact handling of the upper boundary initialization. Furthermore, this type of error model over the stratosphere also holds reasonably well for the other retrieval products (see Figure 4 and Figures 6–8, middle panels), with s_{utls} adjusted and H_{strat} fit to the empirical data of those products.

[53] The reason for an exponential function fitting well lies in the physical nature of the refractivity error. The absolute refractivity error at strato-/mesosphere heights is approximately constant, with random noise being the dominating error source at excess phase path level, propagating almost linearly to bending angle and refractivity level [e.g., *Kursinski et al.*, 1997]. Since refractivity falls off exponentially with an atmospheric scale height of around 7 km, the relative refractivity error then also shows an exponential fall off. The deviation of the fitted stratospheric error scale height (~11 km) from the atmospheric scale height (~7 km) is mainly due to the application of the statistical optimization at bending angle level, which damps the error increase with height and thus leads to an increased error scale height.

[54] From the upper troposphere level downwards, the relative refractivity error is found to increase closely proportional to an inverse-height law ("$1/z^p$" law, with p = 1), which captures the increasing influence of horizontal variability errors [e.g., *Kursinski et al.*, 1997; *Foelsche and Kirchengast*, 2004a]. In fitting our global refractivity results with p = 1 ("$1/z$") within 2–14 km, we found a best-fit value s_0 = 4.5% for the ~1 km error, corresponding to an error of ~2% at 2 km. Figure 10, top-middle panel, illustrates the fit. From our fit we can recommend use of equation (1a) down to 2 km, the physics-based limit we see is that it should be used only within the free troposphere above the planetary boundary layer, i.e., in general above 1–2 km only. Regarding other retrieval products, this "$1/z^p$" model is applicable also to bending angle (Figure 4), where equation (1a) with p = 3 ("$1/z^3$" dependence) fits well down to an impact height of 4 km. For the other parameters (after hydrostatic integration, optimal estimation) the structure is less simple. However, error models for refractivity and bending angle are of main interest for data assimilation purposes.

[55] Equations (1a)–(1c) can be used, via re-adjusting/-scaling/-fitting the parameters $z_{troptop}$, $z_{stratbot}$, s_{utls}, H_{strat}, s_0, and p, to similarly approximate any other error profile data. An example is scaling to current RO data such as CHAMP data, which furnish somewhat less accuracy than the GRAS-type system baselined here. For this case we suggest that adjusting s_{utls} to 0.3–0.5% and re-scaling or re-fitting H_{strat} to near 15 km, keeping the other parameters the same, captures the main differences in global and annual mean refractivity errors between GRAS-type and CHAMP-type systems. Given sufficiently resolved error analysis data sets, regional and seasonal dependences can also be estimated and modeled by varying the parameters accordingly.

[56] The second aspect of the error covariance matrices is the correlation structure. We tried to fit different functions (exponential, Gaussian, Mexican Hat) to match the correlation structure, the ones presented were chosen depending on the smallest fit residuum. We approximated the shape of the refractivity error correlation functions at an L60 height grid by an exponential drop-off with a correlation length L = 2 km in the troposphere (up to 15 km), linearly decreasing to L = 1 km at 50 km height. Figure 10, right panel, illustrates this exponential drop-off model with height-varying L. Combining the standard deviations from the model above with this error correlation modeling, we can write the global refractivity error covariance matrix, **S**, as

$$\mathbf{S} = S_{ij} = s_i s_j * \exp\left(-\frac{|z_i - z_j|}{L(z)}\right), \quad (2)$$

where $L(z)$ is the (linearly) height dependent correlation length, z_i and z_j are the height levels between which the correlation is measured, s_i and s_j are the standard deviations (from equation (1)) at z_i and z_j, respectively, and S_{ij} are the covariance elements of **S**. Considering use of equation (2) also for error covariance matrices of other retrieval products, it is found that it also reasonably applies to fit bending angle covariance matrices at the L60 grid, whereby in this case correlation lengths appear to be as small as 0.5–1 km (see Figure 4). For the parameters further retrieved from refractivity, correlation structure is more involved, as already noted above also for the standard deviation structure in the troposphere (Figures 6–8).

[57] As described in section 5, negative correlations in refractivity can hardly be seen at an L60 height grid but can be resolved at a finer grid. Since these negative correlations are most pronounced in the low latitude ensemble at lower

to middle stratospheric heights we also tried to model error correlation functions including anti-correlation features at a higher vertical resolution, using about 90 height levels instead of 60 levels. For this grid we just used every 5th height level of the original retrieved profiles resulting in 92 height levels from 2 km to 50 km. Figure 10, bottom panels, illustrates the results for the low latitude (middle panel) and global ensemble (right panel), respectively.

[58] For this alternative modeling of **S**, we used a Mexican Hat function of the form,

$$\mathbf{S} = S_{ij} = s_i s_j \cdot \left(1 - \frac{(z_i - z_j)^2}{(c \cdot L)^2}\right) \cdot \exp\left(-\frac{(z_i - z_j)^2}{L^2}\right), \qquad (3)$$

where, for the results of Figure 10, L was used as above ($L = L(z)$). For the global ensemble the stretching factor c was set to $c = 2$, and for the low latitude ensemble it was set to $c = 2$ below and to c = 0.8 above the tropopause level (15 km), respectively. Since the Mexican Hat function implies a Gaussian shape of the correlation structure, equation (3) is not generally invertible. This can be overcome by approximating the Gaussian factor, $f = \exp\left(-\frac{(z_i - z_j)^2}{L^2}\right)$, in equation (3) with a 5th order polynomial function as described by *Gaspari and Cohn* [1999]. Using a re-scaled height z defined by

$$z = \left|\frac{(z_i - z_j) \cdot \sqrt{0.3} \cdot \sqrt{2}}{L}\right|, \qquad (4)$$

an approximate function $\tilde{f}$ can be written in the form,

$$\begin{aligned} \tilde{f} &= -\frac{z^5}{4} + \frac{z^4}{2} + \frac{5z^3}{8} - \frac{5z^2}{2} + 1, \quad 0 \le z \le 1, \\ \tilde{f} &= \frac{z^5}{12} - \frac{z^4}{2} + \frac{5z^3}{8} + \frac{5z^2}{3} - 5z + 4 - \frac{2}{3z}, \quad 1 < z \le 2. \end{aligned} \qquad (5)$$

Substituting the Gaussian factor f with this approximate factor $\tilde{f}$, we can write **S** as

$$\mathbf{S} = S_{ij} = s_i s_j \cdot \left(1 - \frac{(z_i - z_j)^2}{(c \cdot L)^2}\right) \cdot \tilde{f}, \qquad (6)$$

which is robustly invertible and delivers closely the same result as equation (3). Since bending angle error correlation structure shows more anti-correlation than refractivity (see discussion in section 5), equation (6) might also be adequate for modeling bending angle error correlations.

[59] As can be seen in Figure 10, bottom panels, the empirical error correlation values at the higher vertical resolution are approximated fairly well with the Mexican Hat model. For the low latitude ensemble (middle panel) the anti-correlation structures are reasonably captured, while in the global ensemble (right panel) the negative correlations are smoothed already and consequently not modeled. This finding points also to the fact that use of global covariance matrices, and thereby disregarding latitudinal, and other, dependences of errors, is a rather crude approximation, in particular so at high vertical resolution. On the other hand, data assimilation systems are often not that sensitive to the precise formulation of the observation error covariance matrices employed, as long as it is reasonably adequate, but the exact sensitivities have to be individually investigated for each specific system (e.g., C. Marquardt and S. B. Healy, Met Office, Exeter, UK, private communications, 2003).

7. Summary, Conclusions, and Outlook

[60] We presented results of an empirical error analysis for GNSS radio occultation (RO) data based on end-to-end forward-inverse simulations of an ensemble of RO events under fairly realistic modeling conditions. Starting with information on excess phase and Doppler errors, which are representative of the expected performance of the upcoming METOP/GRAS GPS RO data, we provided a comprehensive error estimation for the atmospheric retrieval products bending angle, refractivity, pressure, geopotential height, temperature, and specific humidity.

[61] The ensemble-based empirical error analysis approach allowed to avoid making assumptions such as linearity, un-biasedness, dry troposphere, a few standard atmospheric conditions only, spherically symmetric atmosphere, and no ionosphere, which were to varying degrees involved in previous error studies [e.g., *Kursinski et al.*, 1997; *Syndergaard*, 1999; *Palmer et al.*, 2000; *Healy and Eyre*, 2000; *Rieder and Kirchengast*, 2001b]. One limitation of realism also in this study is the use of geometric optics ray-tracing in the forward modeling, which implies that multipath and super-refraction conditions in the lower troposphere are not accounted for; all simulated profiles in the statistical ensembles stop above such conditions if they encounter them. Future consolidation of estimates will thus be valuable in particular below about 3 km at low latitudes, where multipath and super-refraction effects can play the largest role. Furthermore, small scale atmospheric and ionospheric structures are not accounted for, being an additional contribution to the error budget of real data sets.

[62] The present study advanced the earlier results in that it provided, based on the quasi-realistic data sets, both complete error covariance estimates (standard deviation profiles and correlation functions) and bias profile estimates, for all parameters from bending angle to humidity. Understanding of residual biases in retrievals from the self-calibrated and thus nominally un-biased raw RO data, and subsequent efforts to mitigate them, is crucial for climate applications.

[63] Where comparable, the results of this study are consistent with the findings of theoretical studies [*Syndergaard*, 1999; *Rieder and Kirchengast*, 2001b]. When comparing and interpreting them in relation to the findings of the theoretical studies, one has to be aware of the differences between the studies, however, especially of the limiting assumptions in the theoretical studies like un-biasedness and dry air assumptions, but also of retrieval algorithm differences such as different resolution-accuracy trade-offs and background error specifications. This way the theoretical results obtained under more simplified conditions proved a valuable aid in the interpretation of the empirical results under more realistic conditions.

[64] The results, furthermore, expanded and consolidated the rms error estimates obtained by *Kursinski et al.* [1997]

based on a more simplified analysis. The empirically derived standard deviations of refractivity, geopotential height and temperature agree well with the rms errors estimated by *Kursinski et al.* [1997] in the upper troposphere and lower stratosphere; in lower troposphere refractivity we found a twice as large error due to the more realistic horizontally variable fields used in the present study. *Kursinski et al.* [1997] also looked into error budget components not addressed in this study on total retrieval errors. An error budget analysis for a GRAS-type receiving system was recently performed by *Ramsauer and Kirchengast* [2001].

[65] The estimated bias profiles confirmed the high climate monitoring utility of RO data but also pointed to further improvement potential in the retrieval algorithms, especially related to the high-altitude initialization. In general, residual biases are found negligible below about 30 km in all data products and increasingly relevant throughout the upper stratosphere. More specifically, bending angle and refractivity biases start to become appreciable (systematically >0.25%) close to the stratopause only. Appreciable pressure, geopotential height and temperature biases are found to extend about 2 scale heights ($\sim$12–15 km) lower into the stratosphere than those of refractivity, being smallest at mid latitudes and reaching down to below 30 km into the lower stratosphere at high latitudes. These biases are caused by residual mesospheric refractivity (equivalently, density) biases carried downward by the hydrostatic integration in the retrieval of pressure from refractivity. The density biases are, in turn, caused by residual mesospheric bending angle biases carried via the Abelian integration from bending angle to refractivity.

[66] This insight implies that further mitigation of upper stratospheric biases can be achieved via improvements in the statistical optimization of bending angles. In this respect an improved bending angle retrieval algorithm was developed by *Gobiet and Kirchengast* [2004], who included a bias correction of background bending angle profiles which led to significant bias reduction, especially at high latitudes [*Gobiet and Kirchengast*, 2004; *Gobiet et al.*, 2004]. An alternative way of bias mitigation in many RO data processing schemes involves a "2nd initialization" at pressure level, i.e., the initialization of the hydrostatic integral at a height within 30–50 km by an a priori model temperature [e.g., *Kursinski et al.*, 1997; *Wickert et al.*, 2004; *Hajj et al.*, 2004]. This approach is problematic if the retrieved profiles target climatological use, since it leads to intricate error characteristics and a priori dependence in the stratospheric profiles down to about 20 km, which threats the crucial climate requirements of un-biasedness and of a clear understanding of the systematic and statistical error properties.

[67] An encouraging result from the climatological point of view is, furthermore, that biases in specific humidity are found small around 5% at all latitudes and heights, except at mid latitudes above 6 km, where biases reach up to 10%. This finding, together with the small biases also found in temperature below 10 km, indicates that optimal estimation (1D-Var) retrieval based on ECMWF short-term forecasts as background can lead to tropospheric humidity and temperature retrievals useful for climatological applications. While there is other approaches still in use, usually based on a priori temperature aiding observed refractivity for humidity retrieval [e.g., *Kursinski et al.*, 1997], we rate 1D-Var the preferable method for humidity and temperature retrieval from GNSS RO refractivity in the troposphere [cf. *Healy and Eyre*, 2000].

[68] Regarding error correlation functions, the results provide insight into covariance propagation under quasi-realistic conditions. The main differences between the empirically estimated correlations and theoretical ones are seen in the troposphere, including broader refractivity error correlation functions due to horizontal variability. The 1 D-Var retrieval, which is applied in the troposphere does not significantly broaden the correlation functions of temperature and humidity compared to the ones of refractivity in this height regime. Negative correlation minima adjacent to the main correlation function peaks of bending angle and refractivity can be hardly resolved on the L60 vertical grid. Nevertheless, they are present and found resolved on a finer 90 level grid; they are found most pronounced at stratospheric heights at low latitudes, where they are comparable to the error correlation features in theoretical studies [*Syndergaard*, 1999; *Rieder and Kirchengast*, 2001b]. The hydrostatic integration process prevents any appreciable negative correlations in pressure, geopotential height, temperature, and humidity error profiles.

[69] We derived simple analytical formulations of refractivity error covariance matrices by closely fitting the empirically estimated matrices. The functional formulations depend on a few sensibly selected adjustment/fitting parameters only. While we provided values for these parameters based on our empirical data sets reflecting GRAS-type performance, the formulations can be used, via re-adjusting/re-scaling/re-fitting the parameters, to approximate any other error estimation data set; as an example, scaling to CHAMP RO data was addressed. Comparison of the formulations with results of an error analysis of CHAMP RO refractivity profiles confirmed their practical utility [*Steiner*, 2004].

[70] The error covariance matrices, especially those for refractivity and bending angle, should be useful for evaluation and proper specification of observational errors in data assimilation systems as well as in optimal estimation parts of retrieval algorithms, i.e., the optimal bending angle estimation part and the 1D-Var temperature and humidity retrieval part. The simple analytical formulations might be of particular convenience for use in large-scale operational data assimilation systems.

[71] In our ongoing work on the topic we build on the heritage of this simulation study and focus on the empirical error analysis of CHAMP RO data with respect to ECMWF analyses and the separate estimation of the ECMWF model error. This will allow the separation of the observation error from the model error and shall lead to the specification of adequate observation error covariance matrices for data assimilation systems as derived from real CHAMP RO data. The results will provide a further test of the utility of the simple error covariance formulations presented here. Meanwhile it is hoped that these, properly adjusted to the characteristic error magnitudes of the respective observing and retrieval systems of interest, will serve as useful approximations for observation error covariance matrices of radio occultation data.

[72] **Acknowledgments.** The authors gratefully acknowledge valuable discussions on the topic with A. Gobiet and A. Löscher (IGAM,

University of Graz, Austria), X.-Y. Huang (NCAR, Boulder, Colorado, USA), S. Syndergaard (UCAR, Boulder, Colorado, USA), C. Marquardt (Met Office, Exeter, UK), and S. Healy (ECMWF, Reading, UK). U. Foelsche (IGAM, University of Graz, Austria) is thanked for the preparation of Figure 2. A.K.S. was funded for this work from the START research award of G.K. financed by the Austrian Ministry for Education, Science, and Culture (BMBWK) and managed under Program Y103-N03 of the Austrian Science Fund (FWF).

References

Anderson, T. W. (1984), *An Introduction to Multivariate Statistical Analysis*, John Wiley, Hoboken, N. J.

Andersson, E., M. Fisher, R. Munro, and A. McNally (2000), Diagnosis of background errors for radiances and other observable quantities in a variational data assimilation scheme, and the explanation of a case of poor convergence, *Q. J. R. Meteorol. Soc.*, *126*, 1455–1472.

Collard, A. D., and S. B. Healy (2003), The combined impact of future space-based atmospheric sounding instruments on numerical weather-prediction analysis fields: A simulation study, *Q. J. R. Meteorol. Soc.*, *129*, 2741–2760.

Derber, J., and F. Bouttier (1999), A reformulation of the background error covariance in the ECMWF global data assimilation system, *Tellus, Ser. A*, *51*, 195–221.

Edwards, P. G., and D. Pawlak (2000), Metop: The space segment for Eumetsat's Polar System, *ESA Bull.*, *102*, 6–18.

ESA/EUMETSAT (1998), The GRAS instrument on METOP, *ESA/EUMET-SAT Rep. ESA VR/3021/PI, EUMETSAT EPS/MIS/IN/9*, 38 pp., Noordwijk, Netherlands.

Eyre, J. R. (1994), Assimilation of radio occultation measurements into a numerical weather prediction system, *ECMWF Tech. Memo. 199*, Eur. Cent. for Medium-Range Weather Forecasts, Reading, UK.

Fjeldbo, G., and V. R. Eshleman (1965), The bistatic radar-occultation method for the study of planetary atmospheres, *J. Geophys. Res.*, *70*, 3217–3225.

Fjeldbo, G., and V. R. Eshleman (1969), The atmosphere of Venus as studied with the Mariner 5 dual radio-frequency occultation experiment, *Radio Sci.*, *4*, 879–897.

Foelsche, U., and G. Kirchengast (2004a), Sensitivity of GNSS radio occultation data to horizontal variability in the troposphere, *Phys. Chem. Earth*, *29*, 225–240.

Foelsche, U., and G. Kirchengast (2004b), Sensitivity of GNSS radio occultation profiles to horizontal variability in the troposphere: A simulation study, in *Occultations for Probing Atmosphere and Climate*, edited by G. Kirchengast et al., pp. 127–136, Springer, New York.

Foelsche, U., G. Kirchengast, and A. K. Steiner (2003), Global climate monitoring based on CHAMP/GPS radio occultation data, in *First CHAMP Mission Results for Gravity, Magnetic and Atmospheric Studies*, edited by C. Reigber et al., pp. 397–407, Springer, New York.

Foelsche, U., A. Gobiet, A. Löscher, G. Kirchengast, A. K. Steiner, J. Wickert, and T. Schmidt (2005), The CHAMPCLIM project: An overview, in *Earth Observation With CHAMP - Results From Three Years in Orbit*, edited by C. Reigber et al., pp. 615–620, Springer, New York.

Gaspari, G., and S. E. Cohn (1999), Construction of correlation functions in two and three dimensions, *Q. J. R. Meteorol. Soc.*, *125*, 723–757.

GCOS (2003), The second report on the adequacy of the global observing systems for climate in support of the UNFCCC, *WMO/TD 1143*, 74 pp., World Meteorol. Org., Geneva, Switzerland.

Gobiet, A., and G. Kirchengast (2002), Sensitivity of atmospheric profiles retrieved from GNSS occultation data to ionospheric residual and high-altitude initialization errors, *Tech. Rep. ESA/ESTEC 1/2002*, 56 pp., Inst. for Geophys., Astrophys., and Meteorol., Univ. of Graz, Graz, Austria. (Available at http://www.uni-graz.at/igam-arsclisys/publications/publ2002/AGandGK-IGAMTechRepfESA-58p-n1y2002.pdf)

Gobiet, A., and G. Kirchengast (2004), Advancements of GNSS radio occultation retrieval in the upper stratosphere for optimal climate monitoring utility, *J. Geophys. Res.*, *109*, D24110, doi:10.1029/2004JD005117.

Gobiet, A., G. Kirchengast, J. Wickert, C. Retscher, D.-Y. Wang, and A. Hauchecorne (2004), Evaluation of stratospheric radio occultation retrieval using data from CHAMP, MIPAS, GOMOS, and ECMWF analysis fields, in *Earth Observation With CHAMP - Results From Three Years in Orbit*, edited by C. Reigber et al., pp. 531–536, Springer, New York.

Gorbunov, M. E. (2002), Ionospheric correction and statistical optimization of radio occultation data, *Radio Sci.*, *37*(5), 1084, doi:10.1029/2000RS002370.

Hajj, G. A., E. R. Kursinski, L. J. Romans, W. I. Bertiger, and S. S. Leroy (2002), A technical description of atmospheric sounding by GPS occultation, *J. Atmos. Sol. Terr. Phys.*, *64*, 451–469.

Hajj, G. A., C. O. Ao, P. A. Iijima, D. Kuang, E. R. Kursinski, A. J. Mannucci, T. K. Meehan, L. J. Romans, M. de la Torre Juarez, and T. P. Yunck (2004), CHAMP and SAC-C atmospheric occultation results and intercomparisons, *J. Geophys. Res.*, *109*, D06109, doi:10.1029/2003JD003909.

Healy, S. B. (2001a), Smoothing radio occultation bending angles above 40 km, *Ann. Geophys.*, *19*, 459–468.

Healy, S. B. (2001b), Radio occultation bending angle and impact parameter errors caused by horizontal refractive index gradients in the troposphere: A simulation study, *J. Geophys. Res.*, *106*, 11,875–11,889.

Healy, S. B., and J. R. Eyre (2000), Retrieving temperature, water vapour and surface pressure information from refractive index profiles derived by radio occultation: A simulation study, *Q. J. R. Meteorol. Soc.*, *126*, 1661–1683.

Healy, S. B., A. Jupp, and C. Marquardt (2005), Forecast impact experiment with GPS radio occultation measurements, *Geophys. Res. Lett.*, *32*, L03804, doi:10.1029/2004GL020806.

Hedin, A. E. (1991), Extension of the MSIS thermosphere model into the middle and lower atmosphere, *J. Geophys. Res.*, *96*, 1159–1172.

Hocke, K., G. Kirchengast, and A. K. Steiner (1997), Ionospheric correction and inversion of GNSS occultation data: problems and solutions, *Tech. Rep. ESA/ESTEC 2/1997*, 35 pp., Inst. for Geophys., Astrophys., and Meteorol., Univ. of Graz, Graz, Austria.

Hoeg, P., and G. Kirchengast (2002), ACE+ - Atmospheric and Climate Explorer based on GPS, GALILEO, and LEO-LEO radio occultation (ESA Earth Explorer Opportunity Mission Proposal), *Wissenschaftl. Ber. 14*, 121 pp., Inst. for Geophys., Astrophys., and Meteorol., Univ. of Graz, Graz, Austria. (Available at http://www.uni-graz.at/igam-arsclisys/publications/publ2002/PHoegandGK -IGAMWissBer-No14-121p-y2002.pdf)

Kirchengast, G., and P. Hoeg (2004), The ACE+ Mission: An Atmosphere and Climate Explorer based on GPS, GALILEO, and LEO-LEO radio occultation, in *Occultations for Probing Atmosphere and Climate*, edited by G. Kirchengast et al., pp. 201–220, Springer, New York.

Kirchengast, G., J. Fritzer, and J. Ramsauer (2002), End-to-end GNSS Occultation Performance Simulator Version 4 (EGOPS4) Software User Manual (Overview and Reference Manual), *Tech. Rep. ESA/ESTEC 3/2002*, 472 pp., Inst. for Geophys., Astrophys., and Meteorol., Univ. of Graz, Graz, Austria. (Available at http://www.uni-graz.at/igam-arsclisys/publications/publ2002/GKetal-IGAMTechRepfESA-84pOv-n3y2002.pdf)

Kuo, Y.-H., S. V. Sokolovskiy, R. A. Anthes, and F. Vandenberghe (2000), Assimilation of GPS radio occultation data for numerical weather prediction, *Terr. Atmos. Oceanic Sci.*, *11*(1), 157–186.

Kuo, Y.-H., T.-K. Wee, S. Sokolovskiy, C. Rocken, W. Schreiner, D. Hunt, and A. Anthes (2004), Inversion and error estimation of GPS radio occultation data, *J. Meteorol. Soc. Jpn.*, *82*, 507–531.

Kursinski, E. R., and G. A. Hajj (2001), A comparison of water vapor derived from GPS occultations and global weather analyses, *J. Geophys. Res.*, *106*(D1), 1113–1138.

Kursinski, E. R., et al. (1996), Initial results of radio occultation of Earth's atmosphere using the global positioning system, *Science*, *271*, 1107–1110.

Kursinski, E. R., G. A. Hajj, K. R. Hardy, J. T. Schofield, and R. Linfield (1997), Observing the Earth's atmosphere with radio occultation measurements using the Global Positioning System, *J. Geophys. Res.*, *102*(D19), 23,429–23,465.

Lee, L.-C., C. Rocken, and R. Kursinski (Eds.) (2001), *Applications of Constellation Observing System for Meteorology, Ionosphere, and Climate*, Springer, New York.

Leitinger, R., and G. Kirchengast (1997), Inversion of the plasma signal in GNSS occultations – Simulation studies and sample results, *Acta Geod. Geophys. Hung.*, *32*, 379–394.

Leitinger, R., J. E. Titheridge, G. Kirchengast, and W. Rothleitner (1996), A "simple" global empirical model for the F layer of the ionosphere (in German; English version available from the authors), *Kleinheubacher Ber.*, *39*, 697–704.

Leroy, S. (1997), The measurement of geopotential heights by GPS radio occultation, *J. Geophys. Res.*, *102*(D6), 6971–6986.

Marquardt, C., K. Labitzke, C. Reigber, T. Schmidt, and J. Wickert (2001), An assessment of the quality of GPS/MET radio limb soundings during February 1997, *Phys. Chem. Earth*, *26*, 125–130.

Palmer, P. I., and J. J. Barnett (2001), Application of an optimal estimation inverse method to GPS/MET bending angle observations, *J. Geophys. Res.*, *106*(D15), 17,147–17,160, doi:10.1029/2001JD900205.

Palmer, P. I., J. J. Barnett, J. R. Eyre, and S. B. Healy (2000), A nonlinear optimal estimation inverse method for radio occultation measurements of temperature, humidity, and surface pressure, *J. Geophys. Res.*, *105*(D13), 17,513–17,526.

Ramsauer, J., and G. Kirchengast (2001), Sensitivity of atmospheric profiles retrieved from GNSS radio occultation data to instrumental errors, *Tech. Rep. ESA/ESTEC 6/2001*, 65 pp., Inst. for Geophys., Astrophys.,

and Meteorol., Univ. of Graz, Graz, Austria. (Available at http://www.uni-graz.at/igam-arsclisys/publications/publ2001/JRandGK-IGAMTechRepfESA-62p-n6y2001.pdf)

Reigber, C., H. Lühr, and P. Schwintzer (2002), CHAMP mission status, *Adv. Space Res.*, *30*, 129–134.

Rieder, M. J., and G. Kirchengast (2001a), Error analysis for mesospheric temperature profiling by absorptive occultation sensors, *Ann. Geophys.*, *19*, 71–81.

Rieder, M. J., and G. Kirchengast (2001b), Error analysis and characterization of atmospheric profiles retrieved from GNSS occultation data, *J. Geophys. Res.*, *106*(D23), 31,755–31,770.

Rocken, C., et al. (1997), Analysis and validation of GPS/MET data in the neutral atmosphere, *J. Geophys. Res.*, *102*(D25), 29,849–29,866.

Rocken, C., Y.-H. Kuo, W. S. Schreiner, D. Hunt, S. Sokolovskiy, and C. McCormick (2000), COSMIC system description, *Terr. Atmos. Oceanic Sci.*, *11*(1), 21–52.

Rodgers, C. D. (2000), *Inverse Methods for Atmospheric Sounding: Theory and Practice*, World Sci., Hackensack, N. J.

Schmidt, T., J. Wickert, G. Beyerle, and C. Reigber (2004), Tropical tropopause parameters derived from GPS radio occultation measurements with CHAMP, *J. Geophys. Res.*, *109*, D13105, doi:10.1029/2004JD004566.

Schroeder, T., S. Leroy, M. Stendel, and E. Kaas (2003), Validating the microwave sounding unit stratospheric record using GPS occultation, *Geophys. Res. Lett.*, *30*(14), 1734, doi:10.1029/2003GL017588.

Silvestrin, P., R. Bagge, M. Bonnedal, A. Carlström, J. Christensen, M. Hägg, T. Lindgren, and F. Zangerl (2000), Spaceborne GNSS radio occultation instrumentation for operational applications, paper presented at 13th ION-GPS Meeting, Salt Lake City, Utah.

Sokolovskiy, S., and D. Hunt (1996), Statistical optimization approach for GPS/Met data inversions, paper presented at GPS/Met Workshop, Union Radio Sci. Int., Tucson, Ariz.

Steiner, A. K. (2004a), Error analyses of refractivity profiles retrieved from CHAMP radio occultation data, *DMI Sci. Rep. 04-02*, 19 pp., Dan. Meteorol. Inst., Copenhagen, Denmark. (Available at http://www.uni-graz.at/igam-arsclisys/publications/publ2004/Steiner_DMIreport_2004.pdf)

Steiner, A. K., and G. Kirchengast (2004), Ensemble-based analysis of errors in atmospheric profiles retrieved from GNSS radio occultation data, in *Occultations for Probing Atmosphere and Climate*, edited by G. Kirchengast et al., pp. 149–160, Springer, New York.

Steiner, A. K., G. Kirchengast, and H. P. Ladreiter (1999), Inversion, error analysis, and validation of GPS/MET occultation data, *Ann. Geophys.*, *17*, 122–138.

Steiner, A. K., G. Kirchengast, U. Foelsche, L. Kornblueh, E. Manzini, and L. Bengtsson (2001), GNSS occultation sounding for climate monitoring, *Phys. Chem. Earth A*, *26*, 113–124.

Syndergaard, S. (1999), Retrieval analysis and methodologies in atmospheric limb sounding using the GNSS radio occultation technique, *DMI Sci. Rep. 99-6*, 131 pp., Dan. Meteorol. Inst., Copenhagen, Denmark. (Available at http://www.dmi.dk/dmi/sr99-6.pdf)

Syndergaard, S., D. Flittner, R. Kursinski, D. Feng, B. Herman, and D. Ward (2004), Simulating the influence of horizontal gradients on retrieved profiles from ATOMS occultation measurements – A promising approach for data assimilation, in *Occultations for Probing Atmosphere and Climate*, edited by G. Kirchengast et al., pp. 221–232, Springer, New York.

Vorob'ev, V. V., and T. G. Krasil'nikova (1994), Estimation of the accuracy of the atmospheric refractive index recovery from Doppler shift measurements at frequencies used in the NAVSTAR system, *Phys. Atmos. Ocean*, *29*, 602–609.

Ware, R., et al. (1996), GPS sounding of the atmosphere from low Earth orbit: Preliminary results, *Bull. Am. Meteorol. Soc.*, *77*, 19–40.

Wickert, J., et al. (2001), Atmospheric sounding by GPS radio occultation: First results from CHAMP, *Geophys. Res. Lett.*, *28*, 3263–3266.

Wickert, J., T. Schmidt, G. Beyerle, R. König, C. Reigber, and N. Jakowski (2004), The radio occultation experiment aboard CHAMP: Operational data analysis and validation of vertical atmospheric profiles, *J. Meteorol. Soc. Jpn.*, *82*, 381–395.

Zou, X., B. Wang, H. Liu, R. A. Anthes, T. Matsumura, and Y.-J. Zhu (2000), Use of GPS/MET refraction angles in three-dimensional variational analysis, *Q. J. R. Meteorol. Soc.*, *126*, 3013–3040.

Zou, X., H. Liu, and R. Anthes (2002), A statistical estimate in the calculation of radio occultation bending angles caused by a 2D approximation of ray tracing and the assumption of spherical symmetry of the atmosphere, *J. Atmos. Oceanic Technol.*, *19*, 51–64.

G. Kirchengast and A. K. Steiner, Wegener Center for Climate and Global Change (WegCenter) and Institute for Geophysics, Astrophysics, and Meteorology (IGAM), University of Graz, A-8010 Graz, Austria. (andi.steiner@uni-graz.at)

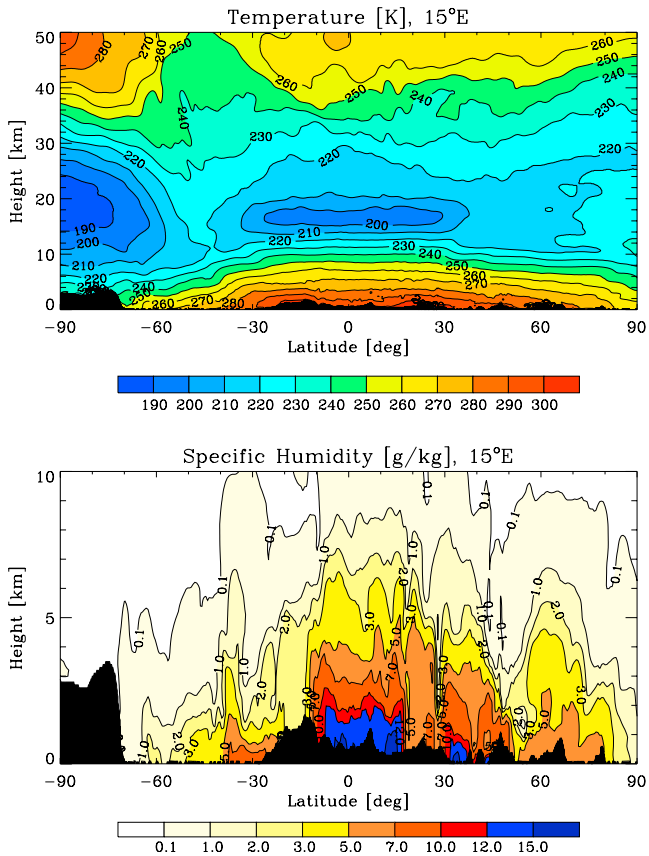

Figure 2. ECMWF T213L50 operational analysis field of September 15, 1999, 12 UT, at 15°E: (top) temperature slice and (bottom) specific humidity slice.